Li leaching from lithium carbonate-primer

An emerging perspective of transport pathway development

Laird, J. S.; Visser, Peter; Ranade, S.; Hughes, A.E.; Terryn, H.; Mol, J. M.C.

DOI
10.1016/j.porgcoat.2019.04.062

Publication date
2019

Document Version
Final published version

Published in
Progress in Organic Coatings

Progress in Organic Coatings 134 (2019) 103–118

Contents lists available at ScienceDirect

Progress in Organic Coatings

journal homepage: www.elsevier.com/locate/porgcoat

Li leaching from Lithium Carbonate-primer: An emerging perspective of transport pathway development

J.S. Laird[a,*], P. Visser[b,c], S. Ranade[d], A.E. Hughes[e,f], H. Terryn[b,g], J.M.C. Mol[b]

[a] School of Physics, Melbourne University, Melbourne, 3000, Australia
[b] Department of Materials Science and Engineering, Delft University of Technology, Mekelweg 2, 2628 CD, Delft, the Netherlands
[c] AkzoNobel, Rijksstraatweg 31, 2171 AJ, Sassenheim, the Netherlands
[d] Department of Metallurgical and Materials Engineering, Indian Institute of Technology Madras, Chennai, Tamil Nadu, 600036, India
[e] CSIRO Minerals Resources, Clayton, Victoria, 3169, Australia
[f] Institute for Frontier Materials, Deakin University, Burwood, Victoria, Australia
[g] Department of Materials and Chemistry, Research Group Electrochemical and Surface Engineering, Vrije Universiteit Brussel, Pleinlaan 2, 1050, Brussels, Belgium

ARTICLE INFO

Keywords:
Lithium
Inhibitor
Corrosion
Leaching
Coating

ABSTRACT

Studies of Li depletion in sections of a Li_2CO_3-primer comprising a polyurethane binder, MgO, TiO_2, $BaSO_4$ in addition to Li_2CO_3, were performed using a combination of particle induced γ-ray and X-ray emission spectroscopies along with SEM/EDS analysis. A mixture of depletion behaviours was observed. At the earliest stages (to around 48 h) initial release was confined to the surface. At longer times (168 h) voids developed deeper into the primer and after 500 h Li_2CO_3 dissolution was observed at places throughout the thickness of the primer to the metal/primer interface. Microscopic transport pathways formed which involved all large inorganic particles. SEM showed that rupture of the polyurethane matrix contributed to network formation. Finite element analysis indicated that rupture may be due to internal stresses around particles isolated in the polyurethane matrix and associated with water uptake. Thus the transport network seemed to be generated by chemical dissolution at the particle/polymer interface and may be enhanced by mechanical degradation due to internal mechanical stresses. The release kinetics of the Li_2CO_3 inhibitor from the primer was followed as a function of time and the data analysed according to a release behaviour of t^n. There was very rapid initial release of Li followed by a slower release of Mg and to a lesser extent Ba. The value of n varied significant with time, but showed a mixture of Fickian release and direct dissolution for Mg and Ba at intermediate times, but transport through a pore network at longer times. The leaching data was interpreted in terms of local transport networks that developed in the primer with time.

1. Introduction

For many years now there has been a drive to remove chromates from corrosion protection for a range of metals in different applications [1–3]. This has led to an extraordinary level of research into inhibitor and coating technology [4–11]. The challenge for chromate replacements is greatest in the aerospace industry where high performance standards are required for new inhibitor systems [11–13].

In recent years, primers containing inorganic Li-based salt as the active inhibitors have received considerable interest as a potential replacement for chromate-based inhibited primers in aerospace applications [14–21]. Recent Tof-SIMS studies have shown that the prevention of corrosion in scribes made through a Li_2CO_3-based model primer is achieved through the formation of a mixture of *pseudo*–boehmite (*p*B) and layered double hydroxide (LDH) components [22]. The protection of the scribe occurs relatively rapidly (within 15 min) [22] through the formation of a mixture of *p*B and LDH both of which contain Li. The ratio of the mixture of phases favours the LDH at longer times. LDH which include hydrotalcites, have been investigated for many years as potential replacements for chromate [23–30] as have *p*Bs [31–34], however, the novelty of the current approach is the incorporation of a simple Li salt into a primer coating where it subsequently leaches into a defect where the mixture of LDH and *p*B forms.

For the protective layer to develop in the scribe in such a short period of time there must be rapid initial release of the inhibitor from the primer. Water uptake and leaching kinetics for inhibited primers have been the subject of a number of studies [4,35–41]. Water uptake is generally quick occurring well within the first few hours of exposure of

* Corresponding author.
E-mail address: tony.hughes@csiro.au (J.S. Laird).

https://doi.org/10.1016/j.porgcoat.2019.04.062
Received 14 January 2019; Received in revised form 31 March 2019; Accepted 22 April 2019
Available online 09 May 2019

a coating to an electrolyte [42–47]. This rapid initial uptake is proposed to occur through the free volume of the polymer [48–50]. This uptake is accompanied by the release of inhibitors which increases with time after the initial water uptake had slowed. The release of inhibitor leads to a depletion zone in the primer. Recent studies [51,52] show that the depth of depletion of an inhibitor may manifest in a range of different ways. It may be a zone of lower inhibitor concentration that moves as a front through the primer (although the "granularity" of this zone will depend on the size of the particles compared to the thickness of the zone and the probing scale). Alternatively, there may be no evenly depleted zone but a front consisting only of fibrils penetrating deep into the primer resulting from the preferential dissolution of connected clusters of particles. The release of inhibitor through these different structures will be goverened by transport kinetics of cation and anion species migrating out to the external electrolyte and also migration of species from the external electrolyte into the primer.

The increase in inhibitor concentration in an electrolyte is often interpreted in terms of a power law behaviour used to describe release kinetics as a function of time (*i.e.* t^n) with a focus around Fickian diffusion where n = 0.5. Many studies find faster release kinetics at short immersion times which are attributed to direct dissolution into solution of the active species from the coating matrix [39,53]. An alternative explanation is that this "fast release" behaviour can be obtained through overlapping release profiles (from individual particles) into solution [36]. At longer release times, a number of studies have found release kinetics that are much slower than Fickian (n < 0.5) (sometimes called pseudo diffusion [53]) and typically around 0.25 [35,37,39,40]. One explanation for this slower release rate behavior is based on transport of inhibitor species through a pore network created in the coating by the dissolution of inhibitor particles [41]. In this scenario n ≈ 0.33. Changing diffusivities (*e.g.* due to pore blockage) may also lead to lower indices [54] so a mixture of behaviours might be expected for inhibitor release from primers.

As noted above, the vast majority of studies of leaching from inhibited primers focus on release kinetics and use electrochemistry to explore leaching behavior [45,55–59]. There are fewer physico-chemical studies which look in detail at the physical and chemical changes in the primer [60] as a result of leaching and fewer still which investigate the role of mechanical degradation resulting from water uptake and inhibitor dissolution on the generation of transport structures in coatings [61,62] although there are some which consider the influence of inorganic fillers in swelling of coatings [63–66]. So, in this paper the authors examine the leaching of components of a Li_2CO_3-loaded polyurethane primer which contains in addition to the inhibitor, the inorganic phases magnesium oxide (MgO), barium sulphate ($BaSO_4$) and titanium dioxide (TiO_2). Characterization studies have been undertaken to follow the depletion of leachable materials from the primer for a range of times up to 500 h exposure to neutral salt spray (NSS). The characterisation was performed using scanning electron microscopy (SEM) with energy dispersive X-ray spectroscopy (EDS), and the nuclear microprobe techniques of proton induced X-ray and γ emission (PIXE and PIGE respectively) spectroscopies. These different techniques have been combined to identify changes that occur in the primer during leaching, particularly the formation of voids that may develop into continuous channels for the transport of inhibitor and other components of the system. Some configurations of void structures and inorganic particles were then used as the basis for finite element analysis (FEA) in an attempt to qualitatively explore how internal stress due to water uptake might influence the generation of those voids within the primer. While FEA has been successfully used in corrosion studies [67], there is little in the way of FEA analyses of coatings containing inorganic phases, apart from some of our previous work [61]. This is probably due to the difficulty of obtaining data for the mechanical properties of the inorganic phases. Finally, leaching of Li, Mg and Ba was followed as a function of immersion time using ICP-AES analyses of leachate solutions. The leaching behavior was interpreted in terms of a t^n behavior and the trends observed in the leaching experiments were interpreted in terms of the physical observations and FEA analyses. On the basis of these data a model is developed on the release of Li_2CO_3 from the polyurethane which involves all the inorganic phases in the coating as well as mechanical stresses.

2. Experimental

2.1. Materials and sample preparation

The coating studied in this work was a high solids primer formulation based on a polyurethane (PU) resin crosslinked with a polyisocyanate curing agent and formulated to a pigment volume concentration (PVC) of 30% as described elsewhere [20]. The PU is a Desmophen® polyester polyol that is used in the performance coatings industry due to its stability under outdoor conditions and chemical resistance. The inorganic pigments included Li_2CO_3, MgO and $BaSO_4$ fillers and TiO_2. Trace element analyses of the various inorganic components of the paint indicated that the $BaSO_4$ contained 0.9%m/m Sr, and small amounts of Si, Ca, Al and Ti. The MgO contained 1500–1900 ppm by weight of Ca, 400–700 ppm by weight K and lesser amounts of other elements (Table 1). The Li_2CO_3 contained alkali metals (Na, K) in the range 400–800 ppm by weight. Particle size distributions for these additives were determined by dispersing in a solvent which was methylethylketone for MgO (d_{50} 8.5 µm), TiO_2 (d_{50} 5.6 µm) and Li_2CO_3 (d_{50} 8.9 µm), where water was used for the $BaSO_4$ (d_{50} 6.5 µm). The $BaSO_4$ particles had the largest particles (d_{99} 50 µm) and the largest spread in particle sizes. The TiO_2 particles were the smallest (d_{99} 14 µm) and slightly smaller than the MgO (d_{99}20 µm). The Li_2CO_3 particle size distribution ranged up to 18 µm (d_{99}18 µm). The solubilities of these inorganics as well as some other related compounds are listed in Table 2 [68].

AA2024-T3 was used as a substrate for the coating; a typical composition for this alloy is reported elsewhere [69]. The AA2024-T3 was prepared by standard anodising according to aerospace requirements (AIPI 02-01-003) at Premium AEROTEC, Bremen Germany. This included the following steps; degrease, alkaline clean, acid desmutting followed by anodising in tartaric-sulphuric acid to produce a 2–3 µm thick oxide layer. Subsequently, the primer was applied by spraying using a high volume low pressure (HVLP) spray gun in a single pass to achieve a dry film thickness of approximately 30 µm; in practice the coating was typically 30–40 µm. Finally the primer was cured for 16 h at 23 °C / 55% RH followed by a 30 min baking cycle at 80 °C.

Neutral salt spray (NSS) exposure was used for physico-chemical analysis, with primer-only samples being exposed for times up to 500 h in a test chamber operated according to ASTM B117. For the leach-rate determination, coupons coated with the primer (surface area of 28 cm^2) were immersed in 50 ml deionized water. Aliquots were taken from the

Table 1
Chemical composition of inorganic additives used in this study.

	Li_2CO_3 mg/kg	TiO_2 %m/m	MgO mg/kg	$BaSO_4$ %m/m
Al	5	1.4	70–77	0.1
Ca	91–98	–	1500–1900	0.1
Na	660–810	–	180–210	0.4
Ba	2	–	2-5	res
Si	–	–	–	0.4
Sr	–	–	–	0.9
Ti	–	–	–	0.1
Zr	–	0.4	–	–
Fe	2	–	73–78	–
Mn	–	–	13–15	
Ni	–	–	5–6	–
K	400–700	–	200–300	–
Mg	39–40	–	–	1

Table 2
Solubilities of various inorganic compounds present in the coatings.

Compound	Solubility in H_2O g/100 ml	Conditions
Li_2CO_3	1.29	25°C
LiOH	12.8	20°C
Li_2SO_4	26.1	20°C
$Mg(OH)_2$	0.00064	25 °C,
	0.004	100 °C
MgO	0.00062	0°C
	0.0086	30 °C
$MgSO_4$	20	20°C
$MgCO_3$	0.01	20°C

solutions and then the solution was replaced with fresh demineralized water after regular intervals from 5 min up to 192 h immersion. The aliquots were acidified with nitric acid to a concentration of 0.1 M and analysed with inductively coupled plasma atomic emission spectroscopy (Arcos NT ICP-AES) using scandium as an internal standard. All leaching measurements were performed in duplicate. For immersion experiments, to ensure sufficient leaching from the primer, 20 parallel cuts with a length of 5 cm (total 100 cm) were scribed into the coating before the immersion. It should be noted that all sections presented in this paper are taken well away from the scribe and did not exhibit any underfilm or through film corrosion after any period of NSS testing.

2.2. Scanning electron microscopy

Scanning electron microscopy was performed on a FEI Quanta 400 field emission, ESEM under two sets of conditions. Imaging and EDS map collection from the primer sections were performed under high vacuum conditions. All samples were coated with around 200 Å of carbon using a carbon electrode evaporation unit. Sample sections were mounted, ground and then polished. Grinding started with SiC papers (320 through to 2400 SiC) followed by polishing on diamond (8, 3, 1, 0.25 µm). All grinding and polishing was performed under either petroleum spirit for SiC papers or Buelher polishing lubricant for diamond stages to avoid unintended dissolution of inhibitor or other particles. It was found that using water or solvents that are azeotropes at the SiC stage resulted in deep loss of Li_2CO_3. Secondary and backscattered electron imaging were performed using beam energies of 10 kV and probe currents of approximately 140 to 145 pA. Quantmaps were generated using a standardless approach, however, the quantmaps were only used to separate the overlapping signals of the Ti K-series lines from the Ba L-series lines using curve fitting.

For the plan view examination of the surface of the primer under SEM, different sample preparation conditions were used. Samples were mounted using double sided carbon tape and carbon dag to form a connecting path between the top surface of the primer and the mounting stub. The samples were then coated with 50 nm of carbon using a coater (Leica EM ACE 600). In order to obtain good spatial resolution needed to find entry pores into the surface of the primer resulting from the dissolution of particles, low voltage imaging at 3 KeV and at a probe current of approximately 100 pA, was performed.

2.3. PIXE and PIGE

PIXE and PIGE have been described in detail previously [15,70]. 3 MeV protons were focused on the sample to approximately 2 µm using a separated quintuplet lens designed for optimal balance between high spatial resolution and maximum beam current. Beam currents were typically in the 0.5–1 nA range. A large area Ge(Li) ϒ-ray detector was placed approximately 5 mm directly behind the sample for a maximum acceptance solid angle. A LiF crystal and pure Al were used for the calibration of the ϒ-ray detector energy axis. For PIXE, a second 100 mm^2 Ge(Li) detector was mounted at 45° to the incident proton beam and 3–4 mm from the sample. A 100 µm thick pure Al filter was placed in front of the detector to reduce overall X-ray intensity. Scan areas chosen for analysis varied, but generally ranged from10 to 50 µm x 200 µm. The analysis depth was approximately 10–20 µm for both methods. For data collection the sample was moved in a grid of points under the proton beam. At each point PIGE and PIXE spectra were collected for each pixel thus forming a hyperspectral data set.

After collection, further data analysis was performed using GeoPIXE [71] where regions of interest (ROI) such as the primer, aluminium alloy or depletion zones were examined in more detail by extracting spectra from each of these ROIs. Both the Li 429 and 478 keV lines were considered for PIGE Li analysis, but only the 429 keV peak was employed due to its greater surface sensitivity [15]. In this case inelastic proton scattering from the nucleus (written ^{7}Li(p, p',ϒ) generates a clear 429 keV ϒ-ray signature, making PIGE an excellent technique for following changes in the Li distribution since Li comes only from the primer in this study [72]. In PIXE the signature K and L-series X-ray emission lines were used for element identification.

2.4. Finite element analysis

To model the influence of internal stresses, finite element analysis (FEA) was adopted to follow the resultant von-Mises stress and shear strain distributions. The ANSYS Student version 19.1 is a software package that enables the modelling of mechanical behaviour of materials in various modes such as under either tensile, compression, or bending loads. The module “Static Structural” was used to simulate the coating and the fillers. All the connections between fillers, coating layers, and substrate were set to “Bonded”. In this instance “bonded” means that the contact surface has maximum friction such that the two bodies are stuck to each other and cannot move with respect to each other. As such the application of force on either one of the bodies will influence the other depending on the latter's mechanical properties, but the latter will not show a physical displacement away from the former body. In practice this may mean that the two dissimilar materials are chemically or mechanically bonded at the interface but there is no formal relationship between the two. A geometric mesh comprising nodes and edges was used to model the sample. This mesh was dependent on certain parameters, where the smoothing option was adjusted to “medium” and the transition to “fast”, along with the span angle center kept at “coarse”. The smoothing enabled a more refined repositioning of the nodes, and the transition determines the rate of the growth (formation) of adjacent elements while the mesh is being formed, with ‘fast’ denoting abrupt changes in properties. Span angle center defines the angular parts formed in a curvature based region, with “coarse” being angles from 91° to 60°. If the fillers have to be viewed in a smaller dimension, or lesser inter-filler distance, the span angle may be kept lower than coarse, so that tiny elements may be formed and point to point strain pattern may be seen. However, in our case, the “coarse” option gave sufficiently understandable results. The posterior side and the bottom of the length of the structure was constricted using the fixed support. A pressure of 0.01 MPa was applied to one of the faces of three of the voids in the model in a direction normal to the face. The results of the analysis have been presented in the form of von-Mises strain and shear strain. The software comes with a library of materials (non-metallic, metallic, gaseous, magnetic, etc.) with their chemical and physical properties, however, none of the inorganics in the primer were listed in the standard database in the software library. So polyurethane foam (flexible) was chosen for the binder in the coating and a mixture of either titanium alloy, magnesium alloy, silicon, and aluminium alloy particles were chosen to represent the inorganic components of the primer. There was no one-to-one correlation with these metals and the inorganics in the primer. The material properties of AA2024-T6 were used to model the AA2024-T3 substrate.

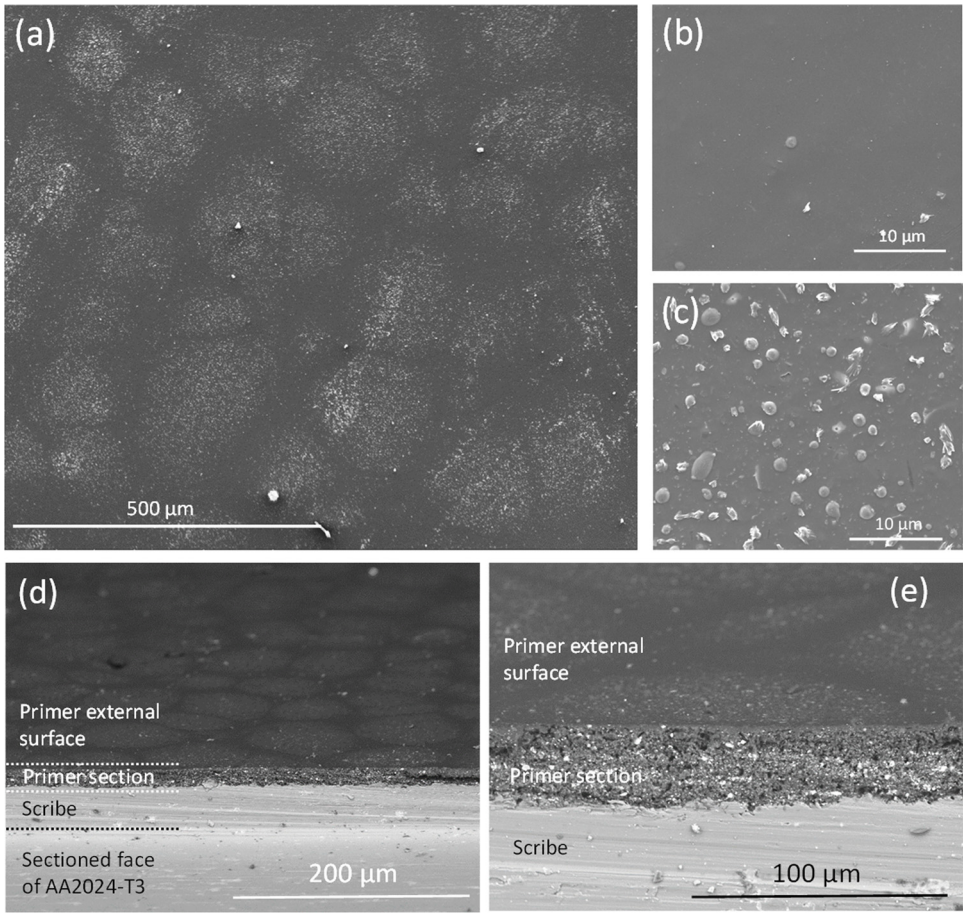

Fig. 1. (a) Low magnification secondary electron image of the primer surface prior to any NSS exposure. There is a cell structure on the surface with regions where there are few to no particles as in (b) and where there are numerous particles as in (c). Backscattered electron images of the scribe (d) without NSS and (e) at higher magnification.

3. Results

3.1. Characterisation of leached primer

3.1.1. External primer surface

Fig. 1(a) shows a low magnification secondary electron image of the external surface of the primer prior to any NSS exposure. A "cell" structure is apparent on the surface where there are regions of high particle density (Fig. 1(c)) which are surrounded by a network containing very few particles as in Fig. 1(b). This structure is thought to be due to the creation of Bénard cells which have been reported to be due to differences in surface tension across the surface of the drying primer [73,74]. Since the samples were also scribed the cut edge of the scribe is also presented in Fig. 1(d) and (e). In the following the focus is on the regions with a high density of particles and not on the cell structure formed by the Bénard cells.

Fig. 2 (a) to (d) shows plan view secondary electron images of the surface of the primer after various exposure times to NSS. Prior to NSS (0 h, Fig. 2 (a)), numerous particles were observed at the surface of the coating within the cells. Many of these particles are Mg-containing as determined using X-ray spectra (EDS), however, as explained in the experimental section these analyses were taken under conditions where the accelerating voltage was only 3 kV, so neither backscatter contrast nor X-ray emission were available to identify the different particles. For the sample without NSS exposure there were virtually no pores detected on the surface of the primer. However after 8 h NSS exposure some pores were evident on the surface (e.g. blue arrows in Fig. 2(b)) and the number increased after 96 h NSS exposure (Fig. 2(c)). These pores probably represent the direct dissolution of either Li_2CO_3 particles or clusters into solution. In addition to the pores there were changes in the appearance of the MgO particles which had an open, coarse porous structure prior to NSS exposure (Fig. 2(e)) which changed to a finer structure (Fig. 2(f)) after 8 h exposure. It is not clear from this data what these changes are related to. After 168 h NSS most of these features had been removed and the number of pores had significantly increased suggesting an increase in the number of particles that had undergone surface dissolution leaving pores behind. The pore density on the external surface, obtained by counting the number of pores per unit area, thus increased during NSS exposure as shown in Fig. 3 indicating leaching of particles from the coating. The particle density in the region within the Bénard cells was a few orders or magnitude larger than the pore density indicating that there were many particles that did not dissolve due to perhaps low solubility or being covered by a thin layer of polyurethane.

3.1.2. Primer sections

Fig. 4 shows backscattered electron images of sections of the primer coatings prior to NSS exposure as well as after 8, 48, 96, 168 and 500 h NSS exposure. The brightest particles in these images are the $BaSO_4$ particles which also contain some Sr [75]. Smaller bright particles are either small $BaSO_4$ or TiO_2 particles. It is not possible to distinguish these particles based on backscatter contrast alone. They can, however, be distinguished using EDS as seen in Fig. 5(a) to (f) for all exposure times and prior to NSS exposure. These maps are composed of multi-element EDS maps with the elemental colour designation shown in the legend at the bottom of each map. Quantitative analysis was performed on the data to generate these maps. This was necessary to separate the overlapping Ti Kα line from the Ba Lα lines using curvefitting. In this fashion the TiO_2 contribution can be made distinct from the $BaSO_4$ contribution. From the combined EDS elemental colour mixing the $BaSO_4$ is a light olive-green, MgO is purple to blue (with the colour variation reflecting a changing composition), the Li_2CO_3 is red because

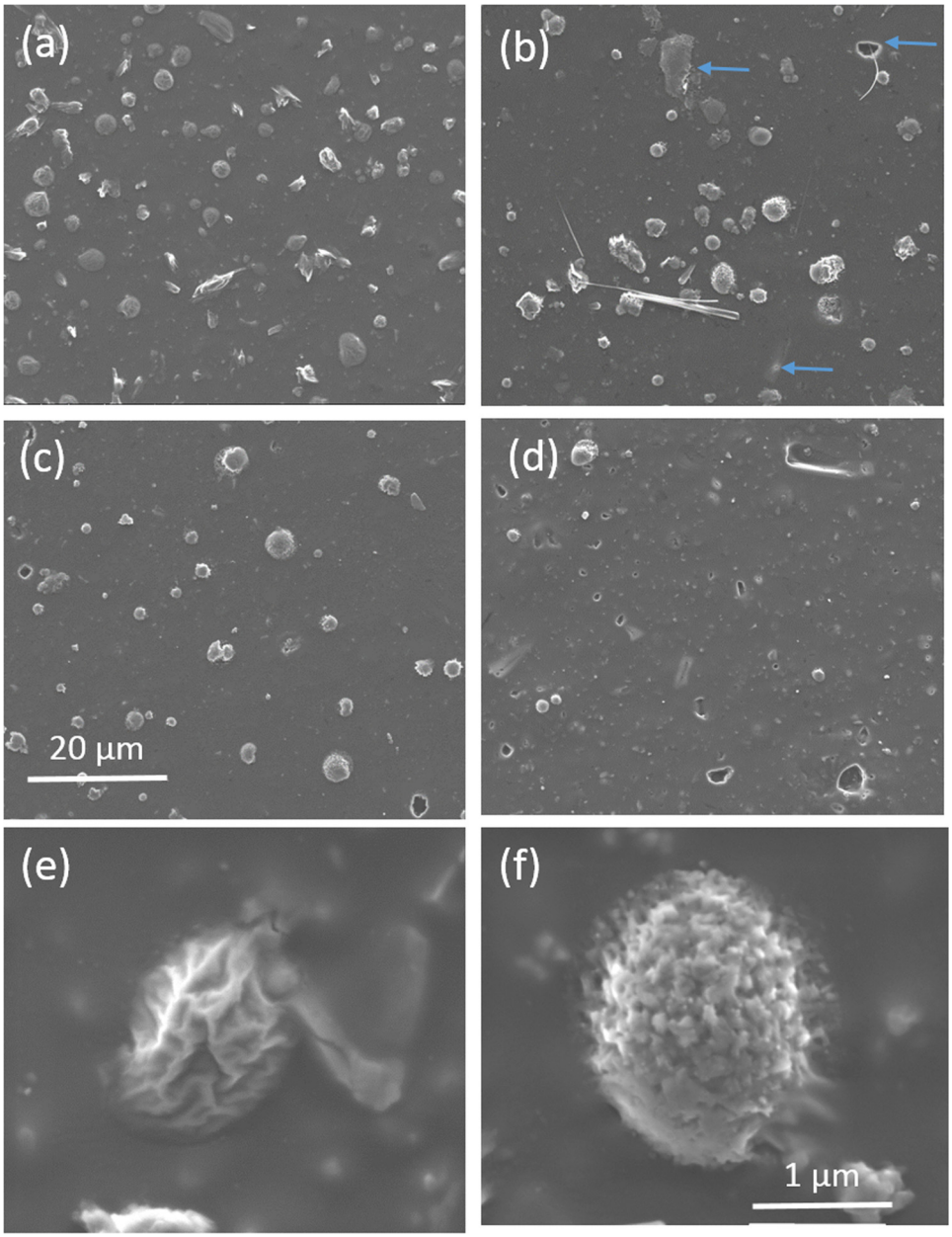

Fig. 2. SEM of top surfaces of coatings (a) before and after (b) 8 h, (c) 96 h and (d) 168 h of NSS. Examples of (e) Mg-oxide/hydroxide prior to NSS and (f) after 8 h NSS. Blue arrows in (b) indicate sites of pores (For interpretation of the references to colour in this figure legend, the reader is referred to the web version of this article.).

it only has an oxygen contribution since Li cannot be detected using standard EDS (and C is not selected). Using only O for identification has previously been established using a combination of PIXE and EDS [75]. The small TiO_2 particles are a salmon-pink colour.

At the shortest exposure time of 8 h only a few pores are evident near the surface. Presumably these pores originate from Li_2CO_3 particles that have dissolved from the surface during initial rapid release as reported by Visser et al. [18]. The lack of extensive pore formation within the surface indicates that Li_2CO_3 dissolution is very local and presumably involves particles that are directly connected to the external electrolyte. The observations are similar for the 48 h sample. However, at 96 h NSS exposure some isolated particles are removed from deeper within the primer which is more apparent in the 168 h and 500 h samples (Fig. 4). There is also apparent delamination/dissolution around subsurface Li_2CO_3 particles as well as other particles such as the MgO and $BaSO_4$. This suggests that all inorganics experience changes at the interface with the polyurethane matrix as a result of NSS exposure.

At the longest NSS exposure times (168 and 500 h), the EDS maps show a loss of Li_2CO_3 (red particles) from the primer (Fig. 5); this is particularly obvious in the 500 h NSS exposure cross section. For the Mg-containing particles there is a colour change from a purple-blue to blue which indicates that these particles have less oxygen in them. (Note: Fig. 5 is a quantmap so colour changes represent concentration changes.) A more detailed determination of the Mg/O ratio for individual particles shows that the reduction in oxygen content occurs early during the NSS exposure as shown in Fig. 6. This may mean that leachable $Mg(OH)_2$ is preferentially dissolved from the MgO particles. The $Mg(OH)_2$ probably forms during air exposure while in storage or the early stages of water uptake.

In summary from the EDS, it seems that Li_2CO_3 is gradually depleted from the primer, initially, by direct dissolution from the surface (or through a thin skin layer) and this is followed by removal at longer

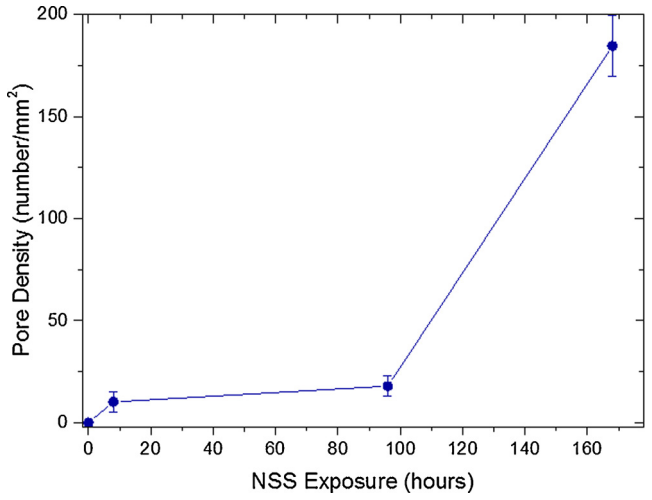

Fig. 3. Pore density in the top surface of the coating as a function of exposure to NSS. Measurements made on plan view such as that shown in Fig. 2.

exposure times from deeper within the primer. At 168 h, a depletion zone from the surface has begun to form and this is clearly seen after 500 h exposure. Other inorganics are also affected by exposure to NSS with the Mg-oxide showing morphological changes on the external surface of the primer after only 8 h as well as compositional changes in the body of the coating. The changes to these particles is extensive after 500 h NSS exposure. Some changes to the $BaSO_4$ particles were observed at 500 h NSS. No changes were observed to the TiO_2 particles.

3.1.3. Depletion depths

In this section PIGE and PIXE are used to examine the Li, Mg, Ba and Ti distributions within the coatings at different NSS exposure times and this information is combined with the EDS and SEM results repoted above.

Fig. 7 gives a general overview of the PIGE and PIXE data which is presented as three colour maps. The Li (red) and Mg (blue) distribution in the primer, and Al (green) from the alloy show the relative positions of the coating with respect to the underlying AA2024-T3 in the PIGE maps (Fig. 7, left). The Li (PIGE - red), Ti (PIXE - green) and Ba (PIXE - blue) distributions (Fig. 7, right) show the distribution of the TiO_2 and $BaSO_4$ with respect to the Li_2CO_3, thus, both sides of Fig. 7 capture all the major inorganic phases within the primer. As reported previously the TiO_2 particles appear to be unaltered by the exposure to NSS, thus its distribution can be used to estimate the primer thickness and by comparison to the other elemental distributions, can be used as a measure of their level of depletion [75]. In the PIXE there appears to be a “Ti-rich” outer layer in the 0 h NSS, although it is most obvious in the 500 h NSS sample. This TiO_2 layer is thought to be due to the smaller Ti particles being better accomodated closer to the surface of the primer than the other larger inorganic particles, although clearly as seen in Fig. 2 some of the larger particles can be seen at the surface of the coating.

The Li-Al-Mg PIGE maps (Fig. 7, left) show that both the Li_2CO_3 and MgO form a well defined, co-incident layer. The maps also show that there are areas where the local concentration of Li_2CO_3 is much lower than elsewhere in the coating (see A and B in Fig. 7(a)). These regions, which also have lower MgO, $BaSO_4$ and TiO_2 levels, penetrate some 20 μm from the external surface towards the primer/metal interface. The distance between A and B is of a similar magnitude to the Bénard cell structure reported in Fig. 1 and Fig. 2. It is important to identify these types of structures when determining depletion depths as they could be mis-interpreted as regions of depletion due to leahcing. On comparing the Li-Ti-Ba maps to the Li-Mg-Al maps, it appears that the layer defined by the Li and Mg profiles are generally thinner than the primer thickness as defined by the Ti map for all NSS exposures. This is most clearly evident for longer times where there is a depletion zone of Li and Mg that penetrates well below the surface as defined by the Ti map as discussed above.

One approach to measure a depletion zone with this data is to create a traverse which is depicted in Fig. 8(a). The area to be analysed is identified by the green rectangle, then a single averaged point is determined from all the pixels along a linescan such as the white line in Fig. 8(a). This process is then repeated for each linescan as a function of distance which in this case is the depth into the coating thus creating a depth profile such as those shown for the sample without exposure to NSS (Fig. 8(b)) and for the sample after 500 h NSS exposure (Fig. 8(c)).

Looking at the depth profile of the sample without NSS exposure, it can be seen that the coating and the AA2024 form well defined regions. The Ba and Ti co-incide whereas the Li seems to increase in intensity only within the coating (the difference between the two is indicated by the pair of black arrows at half height). This is attributed to the larger size of the Li_2CO_3 particles as discussed above.The Mg profile has two steps with the first step (moving from left to right) represents the Mg signal coming from the MgO particles in the coating and the second coming from Mg in the AA2024 which is an alloying component. After 500 h NSS exposure (Fig. 8(c)), both the Li and Mg profiles are quite different from those without NSS exposure. The rise in the Li signal occurs much deeper into the coating and the Mg-step associated with MgO in the primer has receded from the primer/NSS interface towards the metal. The overall Mg signal may also have decreased. Both of these changes indicate that there is leaching from deep within the primer and it involves MgO particles as well as the Li_2CO_3 particles. It is unlikely that trasnport of Mg ions would be through a separate network of voids formed only around MgO particles, therefore it seem logical that both species might be transported through the same network. There also appears to be some depletion of $BaSO_4$ at the longer NSS exposure times (Fig. 8(c)), but not to the same extent as for the Mg and Li. Thus a zone appears to develop where there is removal of many particles which, at the scale of the PIXE, appears as a depleted zone. This zone appears to move into the primer with increasing NSS exposure.

Fig. 9 shows a summary of the different depletion depth measured by different techniques. There are two types of depletion depth presented in the figure. One is the depth of the evenly depleted zone moving from the external surface into the body of the primer. This has been determined from the difference between the width of either the Li or Mg PIGE maps (which coincide) compared to the width of the Ti Kα PIXE map. A separate estimate has been performed for the Ba depletion. It should be emphasised that it is not assumed that this zone comprises very finely dispersed or even molecularly dispersed inhibitor particles which are progressively dissolved as a front moves through the primer. It is simply a region where all the particles (of similar size distributions to elsewhere in the coating) have been dissolved. The depletion depth of Ba is lower than those for Li and Mg. The second depletion depth has been determined from the depth of the deepest pores observed in SEM sections of the primer. An examination of either of these datasets (Fig. 4 (SEM) and Fig. 7 (PIGE/PIXE)) reveals that these different types of depletion depths can vary along sections of the primer and therefore should only be considered as indicative. However, it is clear that at the longer exposure times the development of pores where particles (in whole or in part) have been affected by dissolution occur much deeper in the coating than the advancement of the homogeneously depleted zone. The observation of pores deep in the coating after 500 h most likely reflects the deepest dissolution within particle clusters.

3.2. Development of transport network

Generally, it is expected that void networks for transport can develop in all directions including in the plane of the coating as well as penetrating through the coating from electrolyte to the coating/metal interface. The random direction of network development makes it

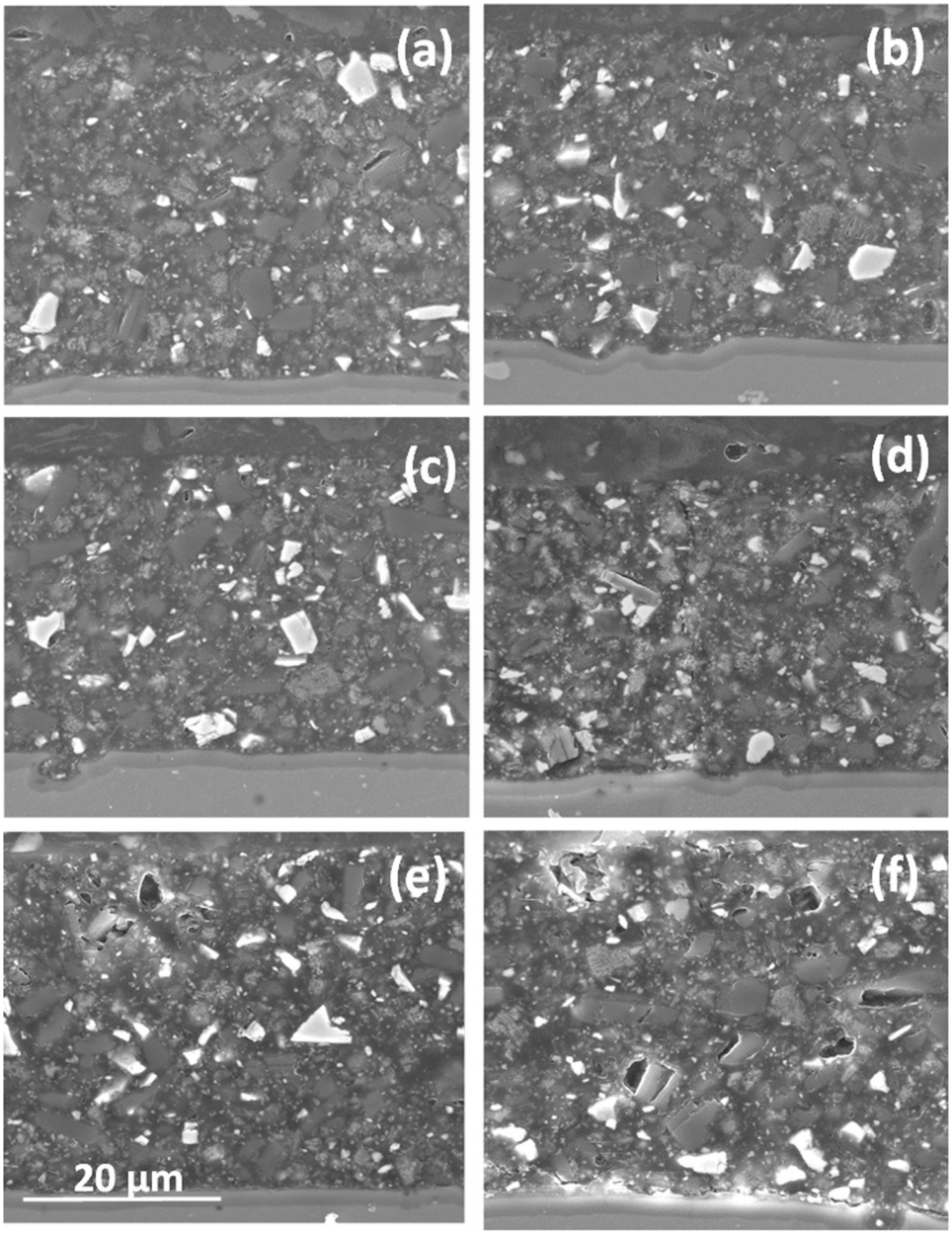

Fig. 4. Secondary electron images of sections of the leached primer as a function of time. (a) 0 h, (b), 8 h, (c) 48 h, (d), 96 h, (e) 168 h and (f) 500 h.

difficult to follow their trajectories without the aid of some 3D imagine technique. Thus in any 2D section only fragments of transport networks are likely to be captured. Nevertheless, some "networks" may simply penetrate the coating in one plane forming a channel from the external surface to the coating/metal interface with such a channel shown in Fig. 10. While these channels have a geometry that may not be typical there is no reason to expect that the chemistry (*e.g.* electrolyte exchange, dissolution phenomena) within it should not be typical of more three dimensional networks. These channels are of interest in that they illustrate the full collection of phenomena that might occur during transport network development.

Fig. 10 shows an example of such a channel after 96 h NSS exposure that has developed through the coating thickness. The mouths of these channels will manifest as pores on the external surface presumably similar to those reported in Fig. 1 and particularly in Fig. 2. Interestingly the channel is not confined to the perimeters of Li_2CO_3 particles but also develops around other inorganic particles in the coating in its propagation from the surface to the metal/primer interface. Close examination of the channel reveals that it is formed by delamination between the matrix and the particles (Type I), but it also penetrates through the polyurethane matrix (Type II). Examples of these Type I (white boxes) and Type II (red boxes) channels are presented in Fig. 10 (d). The presence of a number of different inorganic particles in the channels suggests two things:

(i) network development is not confined to clusters of only Li_2CO_3 particles since there are other inorganic particles observed in the channel. Indeed there are 17 TiO_2 particles, 10 $BaSO_4$ particles, 4 Li_2CO_3 particles and a MgO particle along the length of the channel meaning that the Li_2CO_3 particles only constitute around 13% of the inorganic phases. (Of course the numbers of particles is a poorer indicator than the surface area of the particles in the channel, but this latter quantity is not easy to determine).
(ii) The chemistry of the particles (their solubility) may not be the only factor influencing the propagation of the channel. Indeed the majority of inorganic particles (84%) associated with the channel in

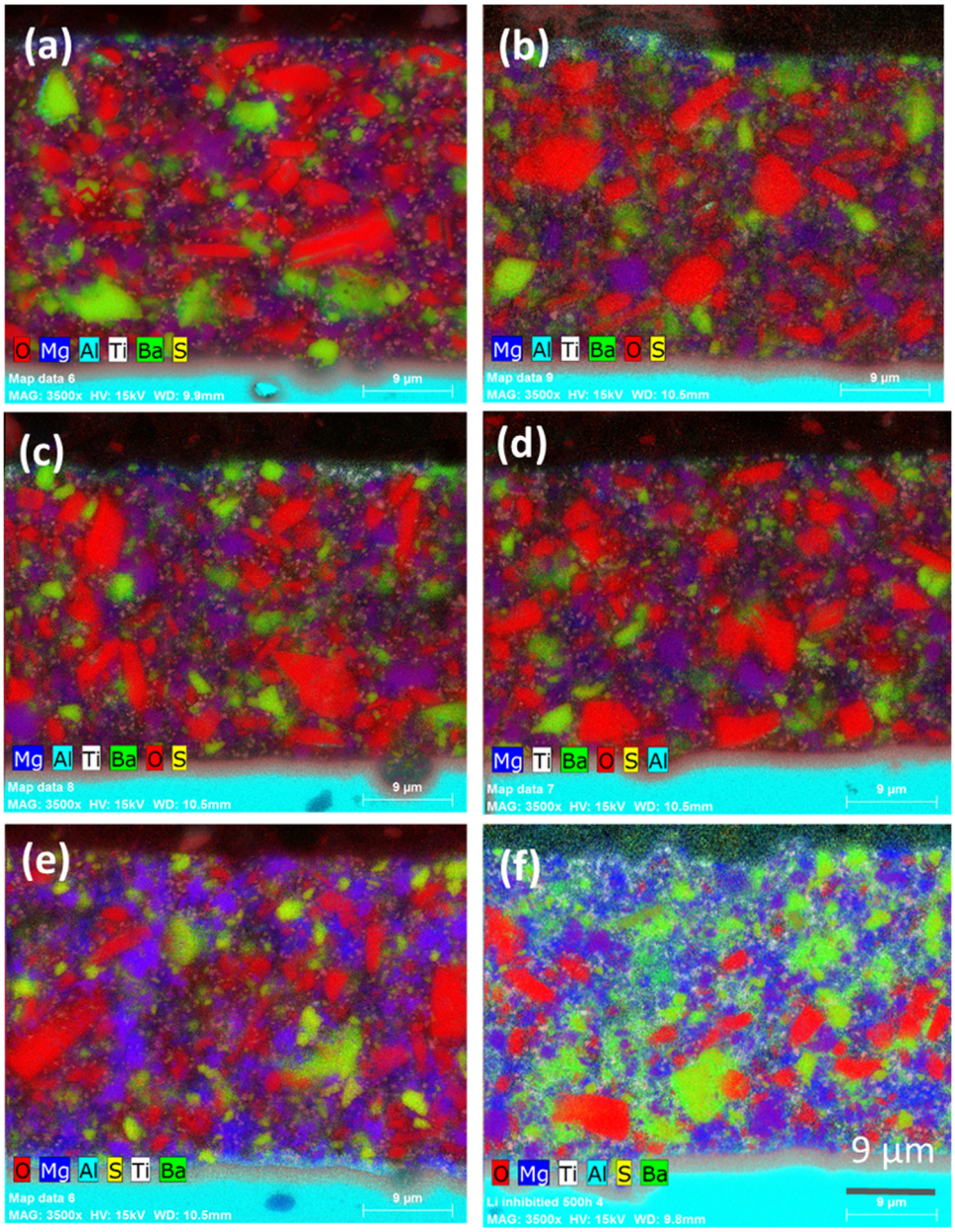

Fig. 5. EDS Quant maps of leaching. (a) 0 h, (b), 8 h, (c) 48 h, (d), 96 h, (e) 168 h and (f) 500 h.

Fig. 10 are the least soluble particles (TiO_2 and $BaSO_4$). For Mg species, if the pH is tending towards alkaline values then their solubility will also be low [76,77]. The images suggest that another mechanism may be involved in network formation. The presence of Type II voids in the channels that penetrate through the polyurethane matrix suggest that internal stresses in the coating also play a role in network formation since this type of void formation cannot be explained on the basis of disbondment due to water penetration to the particle/matrix interface and subsequent reaction.

For parts of the channel in the Type II category one possibility for its formation is that mechanical stresses within the coating cause ruptures which become part of the channel that propagates within the coating. To investigate this possibility a series of voids and sharp particles were built into a finite element analysis (FEA) model of the local environment around the channel in Fig. 10 and stress and strain calculations were performed (Fig. 11). In the model, a number of different inorganic particles were distributed along a path mimicking the actual configuration of particles in Fig. 10 and the blue and yellow lines in (b) and (c) respectively represent the path of the channel. The model also included a number of independent voids which had pressure applied to one internal face at the base of the voids. It is assumed that this pressure arises swelling of inorganic particles resulting from water uptake. At the early stages of exposure to NSS there will be water uptake by the polyurethane through the free volume in the polymer matrix. Free volume sizes (radii) for polyurethane have been reported to be in the vicinity of 2.9–3.7 Å [49,50] whereas water is around 3 Å in diameter. Other ions are too large to diffuse through the polymer at this stage (Table 3) so it can be considered as a selective ion membrane for water [48,78]. Some of the absorbed water will end up at the interface between the polyurethane and the particles where hydrolysis reactions will occur resulting in (i) dissolution of Li_2CO_3 and (ii) formation of hydroxide on MgO particles and possibly some dissolution. Initially this uptake at these sites is probably driven by an osmotic process similar to osmotic blistering where water that is absorbed into the polyurethane through the free volume, reacts with coating components within the

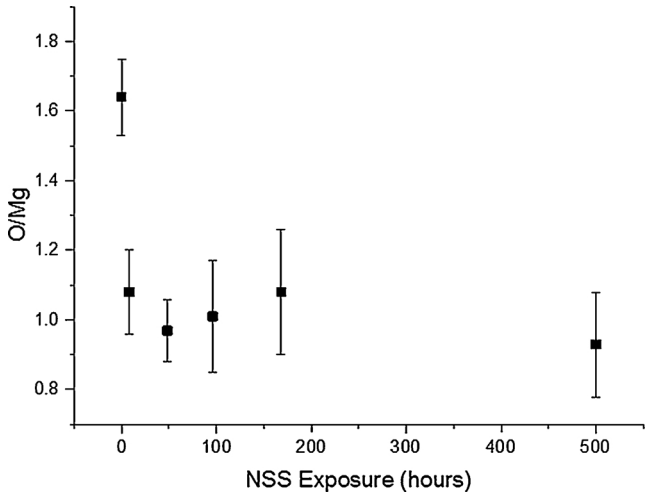

Fig. 6. Mg/O ratio determined from EDS point analyses of multiple particles for each exposure time (minimum of 5 analyses).

primer. In the model in Fig. 11 these voids are fully enclosed and simply mimic what is observed in the cross-section. In reality some of these voids around particles may be filled with gel or electrolyte producing a local swelling around the particles resulting in a hydrostatic pressure due to water uptake within the particles.

Specifically, in Fig. 11 the von Mises strain and shear strain are both increased in the vicinity of the void structures where the internal stress is applied. The von Mises strain is highest at the base of the voids (where the pressure is applied) but this strain is also transferred into the polyurethane matrix by the presence of the particles. A cross-section of the von-Mises strain distribution, depicted in Fig. 11(d), shows the spreading of the high strain region within the plane of the coating, implying that even a small stress may produce an influence over the surrounding polymer. The shear strain is also raised around the inorganic particles near the voids which, if it doesn't cause rupture, will change the free volume characteristic and transport properties through this "modified" polymer. Changing the particles' mechanical properties for the same shapes did not influence the von Mises or shear strains. These results therefore offer an explanation for cracking through the polymer component of the primer. The sharp shape of some voids such as those at the position labelled Ω in Fig. 10(d) indeed suggest

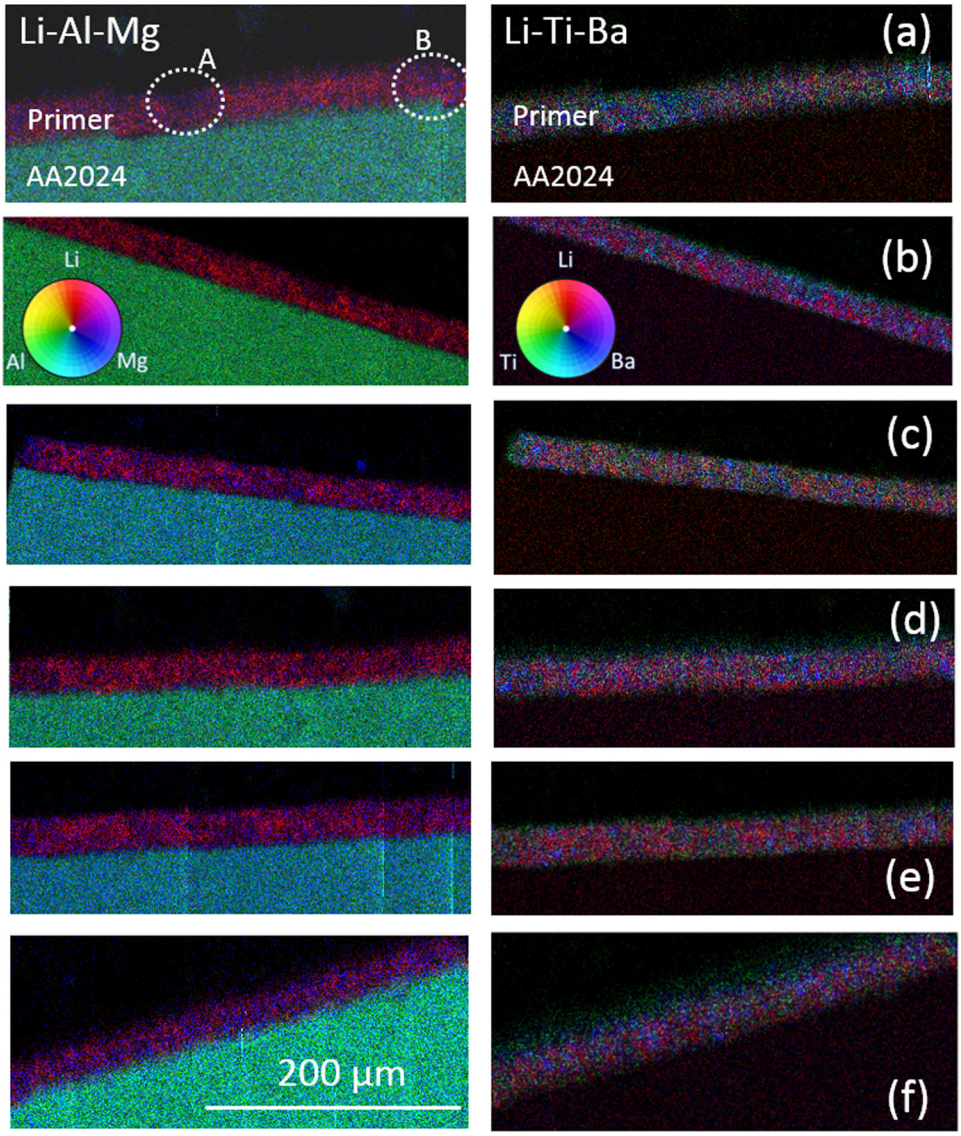

Fig. 7. Left: Li-Al-Mg PIGE 3 Colour maps and right : Li-Ti-Ba mixed PIGE and PIXE 3 Colour maps for (a) no NSS exposure, (b) 8 h, (c) 48 h, (d) 96 h, (e) 168 h and (f) 500 h NSS exposure respectively. Dashed circles in (a)-left indicate regions with very little Li particles.

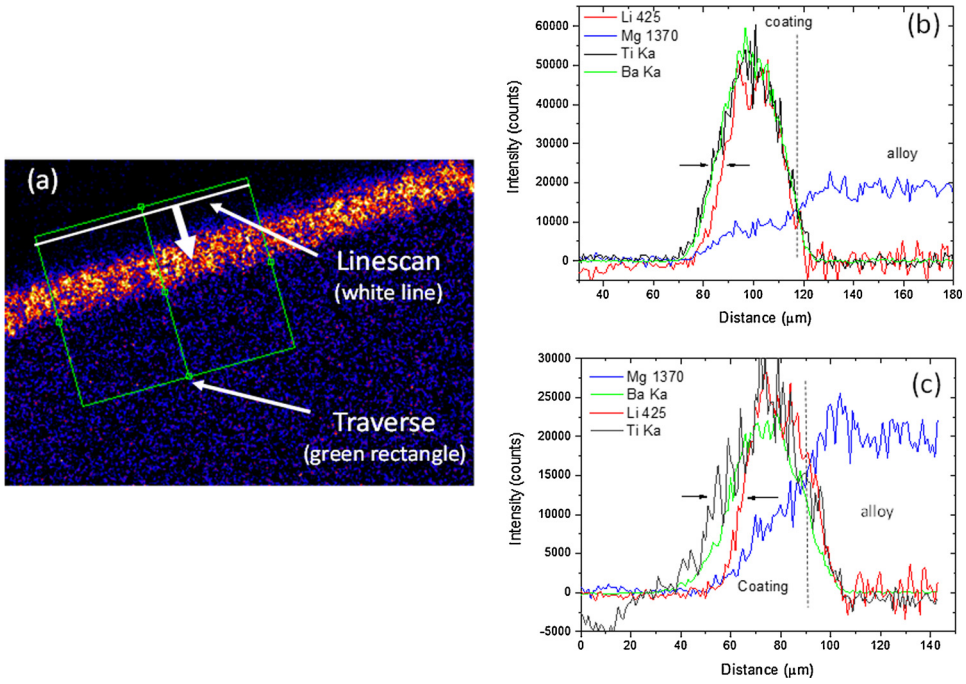

Fig. 8. (a) example of traverse where a region of analysis parallel to the coating surface is chosen (green rectangle) and one single average intensity is determined along a line (white line). This average intensity then represents the intensity in the depth profile. (b) and (c) PIXE (Ba Kα and Ti Kα) and PIGE (Li_{428} and Mg_{1370}) profiles across the primer, (b) Without NSS exposure and (c) after 500 h NSS exposure. The black arrows in (b) and (c) indication the difference at half height of the Ti and Li profiles. The vertical dashed lines in (b) and (c) indicate roughly the boundary between the primer and the metal (For interpretation of the references to colour in this figure legend, the reader is referred to the web version of this article.).

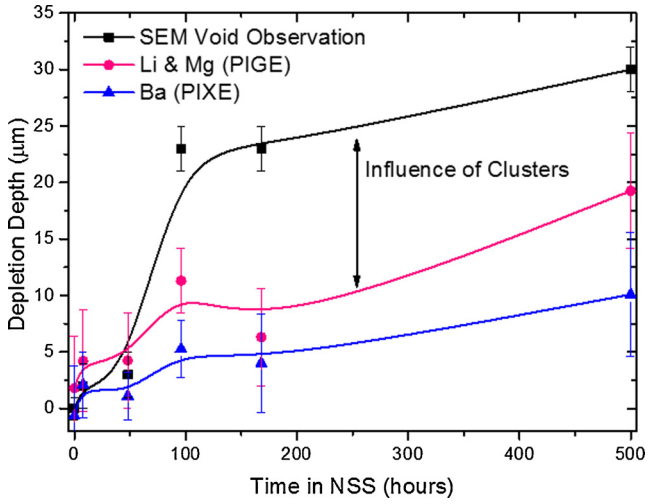

Fig. 9. Different measurements of the leaching depth including deepest observation of pores from SEM and Li and Mg depletion zone determined from Li and Mg PIGE maps.

mechanical rupture.

To explore the influence particles further the model was modified to include particles in a parallel plane behind the visible surface, at a small distance into the interior of the polymer, pointed out by the red arrows in Fig. 12(b). These particles can represent any of the fillers or inhibitor particles. An iso-surface has been shown in Fig. 12(a) and (b), for both the cases, *i.e.*, with and without the additional particles. The original configuration used in Fig. 11 produces a distinct high strain region near the surface due to a cluster of particles as shown by the black arrows in Fig. 12(a) and magnified in Fig. 12(c). The addition of more particles behind the original configuration of particles (red arrows in Fig. 12(b)) changes the strain iso-surface as shown in Fig. 12(b) and magnified in Fig. 12(d). The additional particles leads to a change in the shape of the iso-surface resulting in both linearization and localisation of the strain. Indeed a magnified image in Fig. 12(d) reveals a connection in the high strain regions formed due to the particles in the cross sectional plane and the internal particles. This suggests that the local arrangement of particles plays a defining role in the strains that are induced in the polyurethane and clearly shows that the strain is transferred to the polymer which will result in local changes that might include free volume changes, void formation and channel propagation (these latter two through rupture). It also indicates that while the channels observed in the SEM cross-sections appears to be in a single plane of the X-section, there may be void formation perpendicular to the plane of the channel formed in the coating.

3.3. Leaching behaviour

The previous sections of this paper have focused on changes that occur in the primer as a result of exposure to an NSS environment for different times. The observations have shown some complex behaviors with evidence of direct dissolution, the development of depletion zones at intermediate time as well as evidence of deep attack within the primer for longer times. In this section the leaching behavior is characterized under immersion conditions. The mechanism of release is thought to be similar for both types of experiment, but the kinetics will be faster in NSS due to the removal of electrolyte adjacent to the surface. For example, it was found for a chromate primer that the release during immersion experiments in the first 24 h (33 μg/cm^2 [38]) was around 60% that of NSS exposure (57 μg/cm^2 [52]) for the first 24 h of exposure, but the shape of the release curves was the same.

Fig. 13(a) shows the accumulation of Li, Mg and Ba as a function of exposure time in the leachate solution. For all the reported elements the cumulative amount of material released increases rapidly at short time, but slows at longer times. At the shortest time there was a high level of release of which is likely to be due to immediate, direct dissolution of Li_2CO_3 particles in the surface (including at the scribe) and its high solubility. A significant amount of Mg is also released from the coating during leaching at longer times with the accumulated values in mmol/L shown in Fig. 13(a). Leaching for Mg is much slower than for Li and is still increasing after 500 h exposure. The Mg/Li molar ratio based on the amount released at time *t* minus the amount released at time *(t-1), i.e. the net release/unit time*, is shown in Fig. 13 (b). The Mg/Li ratio starts to show a significant increase towards unity after around 1 h and peaks at around 50 h at a ratio of 1.4 thereafter falling back to 0.6 to 0.8. At these longer times which, as can be seen from the accumulated Li levels, a significant amount of Li has already been released

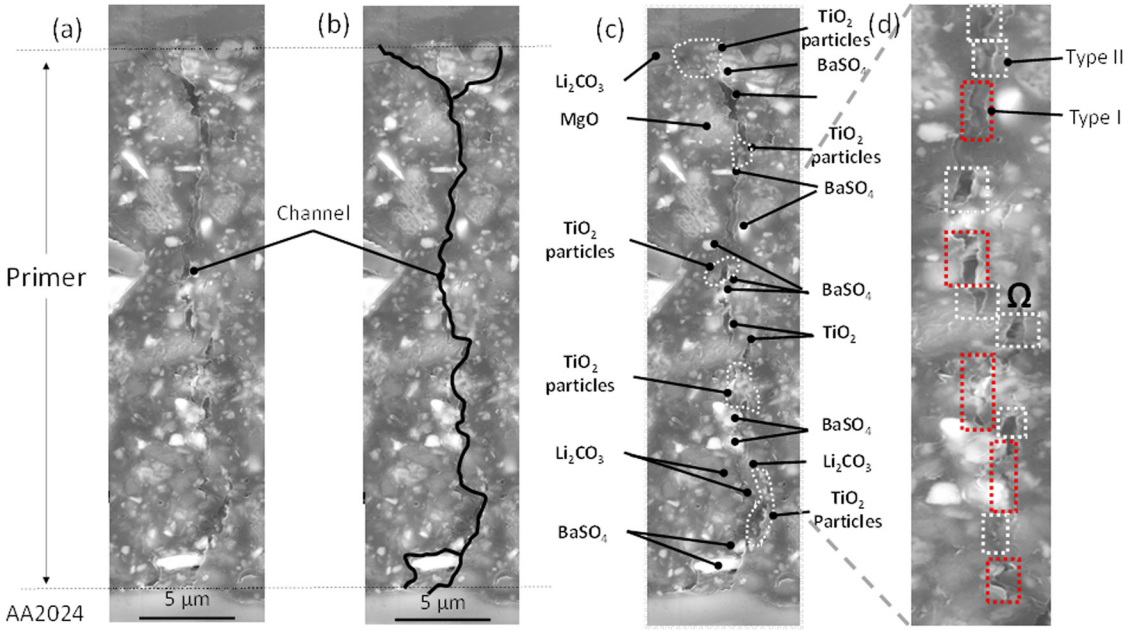

Fig. 10. SEM of an example of a channel through the primer present after 96 h exposure to NSS. (a) image showing just the section and indicating the primer and AA2024 alloy, (b), image with the channel highlighted, (c) image with relevant inorganic phases highlighted and (d)showing examples of Type I (polymer/particles interface) and Type II (though polymer) cracks in the channel.

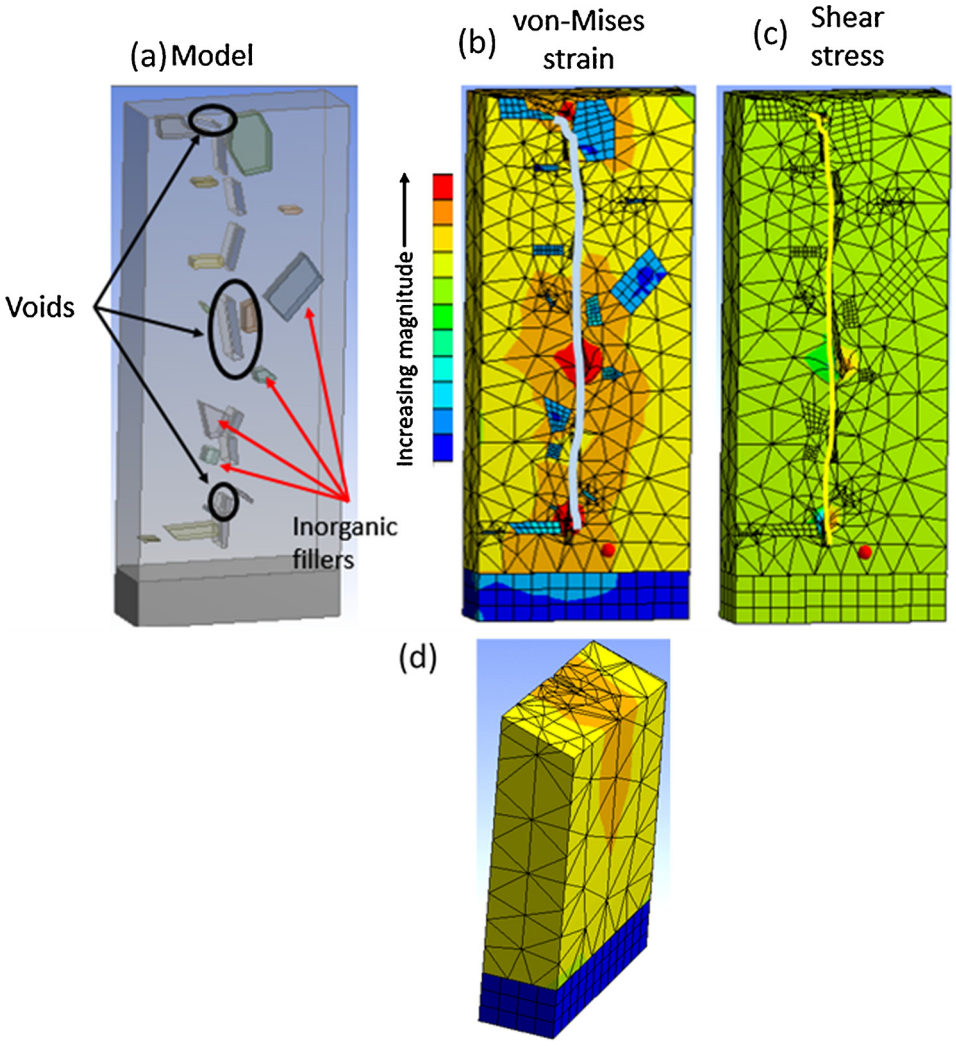

Fig. 11. FEA analysis of stress distributions in the primer. (a) Model of particles in an arrangement reflecting particles in Fig. 10. Circles indicate the position of the cylindrical voids and all coloured shapes are inorganic particles with some highlighted with the red arrows. The pressure has been applied to the bottom face of these voids. (b) von-Mises strain distribution. The blue line is the actual channel path from Fig. 10. (c) shear stress distribution with the yellow line indicating the path of the actual channel. (d) von Mises strain distribution penetration into the film behind the face shown in (b) (For interpretation of the references to colour in this figure legend, the reader is referred to the web version of this article.).

Table 3
Hydrated radii for selected ions after Mahler and Persson [79].

Ion	Hydrated Radius Size (Å)
Cations	
Al^{3+}	4.75
Li^{+}	3.82
Mg^{2+}	4.28
Na^{+}	3.58
Anions	
Cl^{-}	3.32
CO_3^{2-}	3.94
SO_4^{2-}	3.79

(Fig. 13(b)). This shows that Li release precedes Mg release even though the depletion zones overlap as seen in the PIGE results in Fig. 7. There it was concluded that the Li and Mg probably diffuse via the same networks, however, the leaching results show that even if the same networks exist for transport of species, the kinetics of release will also be influenced by the solubility of the particles. Thus in this case the lower solubility of MgO leads to different release kinetics compared to the Li_2CO_3. Both the accumulated Ba release and the Ba/Li molar ratio show a similar behaviour to the Mg release and the Mg/Li molar ratio, but at lower values for both metrics. The similarity of the Mg/Li and Ba/Li curves for accumulated and molar ratios indicates that solubility is not the major limiting factor for release, but that the development of a porous network is the limiting factor.

Leaching data is often interpreted using a power law such as the following equation to distinguish between different leaching behaviours:

$$M = kD_{eff}\,t^{n} \tag{1}$$

Where M is the mass of material released at time t, k is a constant, D_{eff} is an effective diffusion and n is an index that reflects the kinetic behavior dictated by the porosity of the structure from which material is released. For example $n < 0.33$ suggests leaching from a void structure that is fractal in nature [41], $n = 0.5$ reflects Fickian diffusion through the polymer and $n > 0.5$ reflect a significant amount of direct dissolution into the electrolyte [38,39]. This region has also been described by overlapping diffusion fronts [36] or polymer matrix properties [53]. By differentiating Eq. (1) with respect to time and taking the log of both sides the following equation is obtained where n can be calculated directly from the gradient of the a linear fit to the data [39]:

$$log_{10}\left(\frac{dM}{dt}\right) = (n-1)log_{10}(t) + k' \tag{2}$$

where k' is a constant which equals $\log_{10}((n\text{-}1)D_{eff}k)$. The data as represented by Eq. (2) for Li, Mg and Ba are plotted in Fig. 13(c). The gradient of the data is (n-1) from which n can be calculated. It can be seen that the Li release rate decreases markedly with time and largely shows a linear behavior. A linear fit reveals a value of n close to 0.02, indicating that the release very rapidly goes to zero after the initial high release. However, only around 10% of the Li is released during this initial phase and that occurs in the first few hours. This is consistent with the characterization data of samples exposed to an NSS environment reported above where there is still considerable Li carbonate remaining in the coating at 500 h. On the other hand the Mg and Ba leach rate data appears to have three different regions. In Region I the gradient is steep, meaning that n is low for both species.

Fig. 13(d) shows the value of n as a function of time. At $t = 0$ it is assumed that $n = 1$ for Li and Mg (direct dissolution including the scribe) since they have non-zero values after only 5 min exposure, and zero for Ba, *i.e.* no release. In Region II, between 15 min and 24 h (-0.6 and 1.38 on the $\log_{10}$ scale) the leach rates show a similar decline for Mg and Ba as indicated by the dashed line labelled α. Linear fits to this region give indices n between 0.6 and 0.8 (Fig. 13 (d)) and probably represents a mixture of direct dissolution into the leachate solution and Fickian diffusion. (Note n is the same across Region II for Ba and Mg because it is the gradient of the linear fit to data in this region (Fig. 13(c)).) It is in this region that it is expected that Mg (and Ba) are released through common channels created by Li_2CO_3 dissolution and MgO dissolution and mechanical rupture. At the longest times (Region

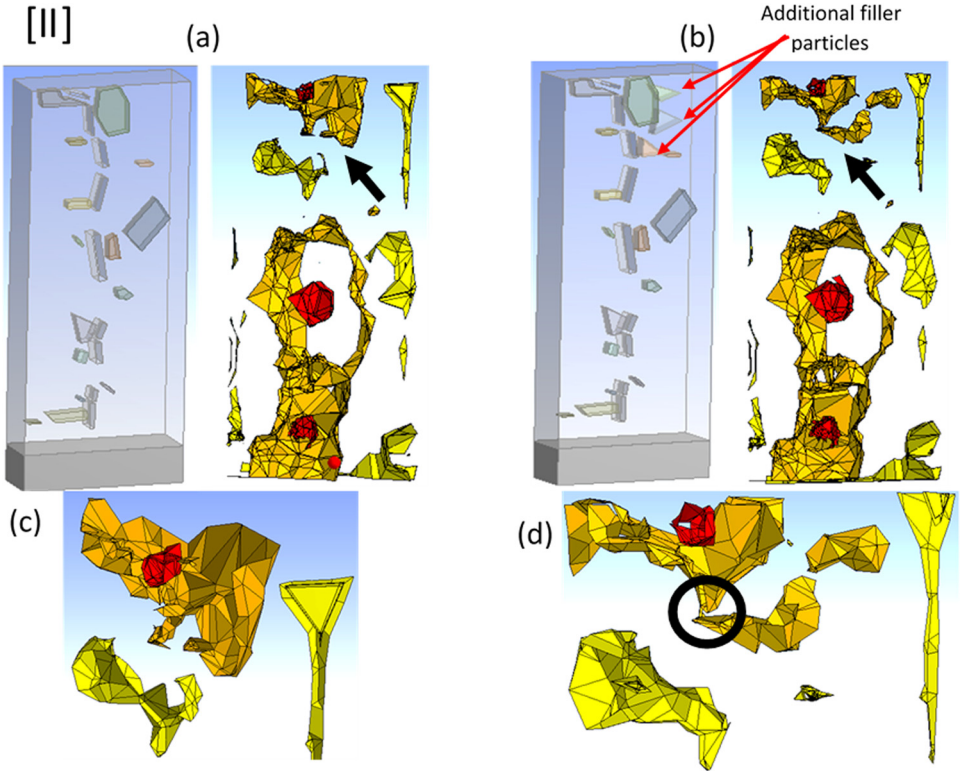

Fig. 12. Comparison of FEA analysis of strain distributions in the primer in Fig. 11 and the primer with additional filler particles at a certain distance inside the thickness parallel to the cross sectional plane. Image (a) depicts circles indicating the position of the cylindrical voids and all coloured shapes are inorganic particles with some highlighted with the red arrows. The pressure has been applied to the bottom face of these voids. (c) and (d) are magnifications of the regions above the black arrows in (a) and (b) respectively (For interpretation of the references to colour in this figure legend, the reader is referred to the web version of this article.).

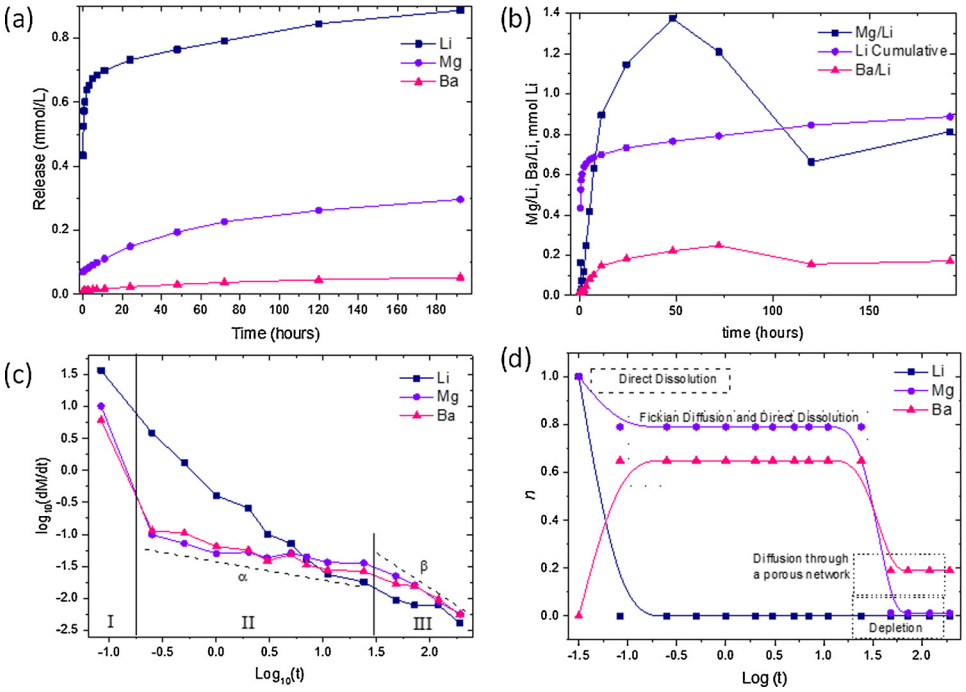

Fig. 13. (a) Cumulative leaching curves (mmol/L) of Li, Mg and Ba from the primer as a function of time. (b) molar ratios for Mg/Li and Ba/Li as a function of time. (c) rate of change of the concentrations (Log_{10}(dM/dt from Eq. (2)) versus Log_{10}(t) for Li, Mg and Ba. Vertical black lines represent boundaries between different leaching regimes (for Ba and Mg) I and II respectively. Dashed lines labelled with α and β are indicative of potentially different gradients in the data. (d) Interpretation of leaching in terms of n (from t^n) as a function of log_{10}(t). This diagram highlights different possible transport mechanisms at different leaching times.

III) the leach rate decreases more rapidly than Region II. A linear fit to this region for the Ba and Mg curves gives a value of *n* of approximately 0.12 and close to zero respectively. In the case of Ba this may represent ongoing dissolution and release through a highly tortuous transport network. Similar low *n* values were reported by Klomjit and Buchheit [35] for chromate release based on low solubility arguments. In summary, there is rapid release of Li whereas the release kinetics for Mg and Ba are slower and show a more complex behavior.

4. Discussion

The leaching and characterisation data presented in this paper can probably be divided into two regimes. To begin, the initial release is likely to be via direct dissolution of Li_2CO_3 particles into solution, which is followed by slower dissolution of MgO (Fig. 14(b)). The initial, high Li release rapidly drops to very low ongoing release with a t^n behaviour where $n = 0.02$ which may be close to exhaustion of leachable Li particles connected to the external surface via a void network. At this stage around 10% of the Li is removed from the coating, so the low release rate suggests that surface and near-surface Li_2CO_3 particles have been largely removed. However, since there are still many deeper Li_2CO_3 particles evident in the cross sections, the data also suggests that transport pathways have not developed further into the primer or perhaps less soluble surface layers have developed on the particles.

Other changes are almost certainly occurring in the primer at the same time. Initially, water will be absorbed through the free volume of the polyurethane similarly to many polymer systems [48,49,80–82]. The free volume of polyurethane has been reported to have a characteristic size (radius) in the vicinity of 3.7 Å [50] which is larger than the diameter of a water molecule at 3.0 Å. The uptake of ions is generally slower with chloride diffusion usually around two orders of magnitude slower than water [48,80]. Therefore transport of both anions and cations through the free volume in the matrix is, initially, unlikely given waters of hydration mean that the overall size is larger than the free volume as can be seen in Table 3 where the hydrated diameter, of all relevant ions, is similar to or slightly larger than the characteristic size of the free volume. Li may even be larger than listed in Table 3 since it has been reported to possibly have a second sphere of waters of hydration [79]. This means that, initially, the polyurethane matrix surrounding particles is not connected to the external surface via any channels and is likely to be acting as an ion selective membrane allowing only water to get to the particle /matrix interface. Thus, at these sites, electrolyte that develops at the interface, as a result of water intrusion, will not be able to diffuse into the surrounding matrix. In membrane technology, there is a well known osmotic effect called dewatering, where water uptake into a polymer membrane is reduced as the external electrolyte concentration increases. This osmotic effect arises due to the difference in activities of water in the polymer and in the external salt [48]. Similarly, in the absence of external pathways, the concentrated electrolyte developed around dissolving inhibitor particles will draw water out of the polyurethane, resulting in swelling around these dissolving particles causing a hydrostatic pressure (Fig. 14(f)). The origin of this swelling is distinct from the swelling of the polymer component which is related to irreversible water uptake (water hydrogen bonded within the polymer component) [83]. The osmotic pressure is assumed to be of a similar order to the swelling pressure which is typically less than 10 MPa [64]. It is the difference between the hydrostatic and osmotic pressures that is the source of the applied force in the FEA. For isolated particles this net force will act in all directions, *i.e.*, it should be isotropic. Thus, while in the FEA modelling the force was applied to the base of voids (*i.e.* in the direction of the polyurethane/metal interface), it could equally lead to rupturing towards the surface of the coating as it could towards the polyurethane/metal interface. Either way the network develops into the primer (Fig. 14(c)).

Once the isolated voids around dissolving inhibitor particles become part of a network connected to the external surface then it is expected that the magnitude of these competing forces will change. In the first instance they may combine to expel electrolyte from the network, or at least redistribute it within the network (Fig. 14(c)). At some stage the osmotic pressure will disappear because the water is more likely to diffuse from the void network rather than through the polyurethane. The pressure due to swelling of the particles is also likely to decrease with the loss of electrolyte from the void network. This will mean that inhibitor release will be dominated by local concentration gradients, (*i.e.*, by chemical potential gradients) associated with the ongoing dissolution of inhibitor particles leading to high local electrolyte concentration in the voids [80].

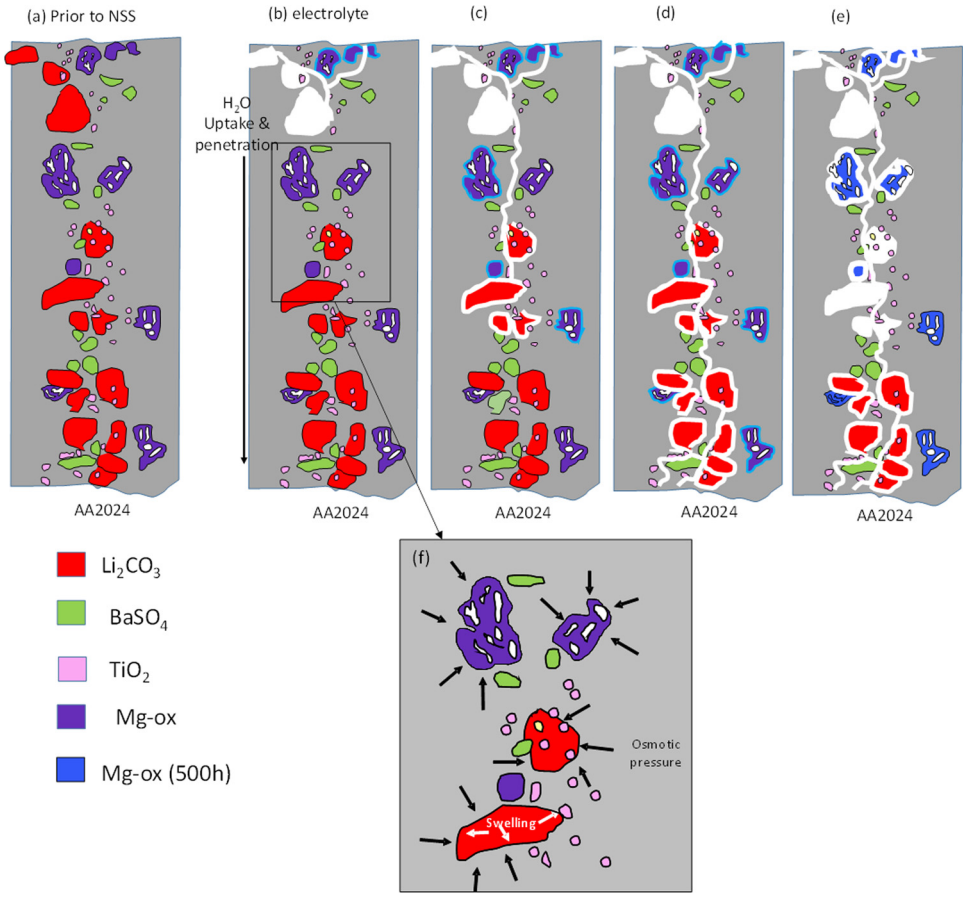

Fig. 14. Model of the development of transport pathways within the primer as a function of time. Colour coding is intended to reflect that of Fig. 5. (a) prior to exposure, (b) early immersion, (c) beginnings of network formation, (d) penetration to metal interface, (e) full penetration plus complete dissolution of some particles including MgO, and (f) osmotic and swelling effects prior to network formation. The lighter blue of Mg-ox (500 h) reflects the EDS Quantmap of the 500 h NSS exposure sample. White represents voids. The pink TiO_2 particles overlaying the Li_2CO_3 particles simply indicate that there are many of these particles present throughout the coating (For interpretation of the references to colour in this figure legend, the reader is referred to the web version of this article.).

As electrolyte exposure increases voids penetrate much deeper into the primer (up to 30 µm) as can be seen in Fig. 9. These are represented by the white space around Li_2CO_3 particles and network penetration (white) to the polymer/metal interface (Fig. 14((d)). This is facilitated by selective dissolution around the surface of particles which may penetrate deeper into the primer where these particles are connected to one another, *i.e.* through clusters connected to the external electrolyte. It is in this regime that the biggest changes are observed on the external surface and within the body of the primer. For example, after 168 h NSS exposure many of the particles at the external surface appear to be removed leaving behind open pores. This change on the external surface is accompanied by pore development within the primer indicating the generation of networks deep within the primer (Fig. 14(d) & (e)). The EDS maps of the cross sections of the primer (Fig. 5) show significant differences between times up to and including 96 h exposure and those above 96 h exposure (168 and 500 h). Above 96 h there is interfacial voids around Li_2CO_3 and MgO particles as well as particle removal.

The data presented in Fig. 10 suggests that the transport pathways for leaching of Li, Ba and Mg are probably not reliant (in Region II at least) on networks that involve the dissolution of Li_2CO_3 particles alone but may well include paths that result from either void formation or delamination around all types of particles as well as the dissolution of Mg-containing particles and to a lesser extent $BaSO_4$ particles. Moreover, the data in Figs. 11 and 12 show that void formation may not just be due to dissolution, but mechanical stresses within the coating may make a contribution via rupture of the polyurethane. On the other hand, the low levels of ongoing release of Li may suggest that dissolution is impeded at the surface of these particles indicating that internal electrolyte conditions may be pivotal in moderating the level of release of the inhibitor perhaps through the formation of less soluble compounds. It is possible that the presence of cations such as Mg^{2+} and to a lesser extent Ba^{2+} (as well as CO_3^{2-}, OH-, SO_4^{2-} ions) may cause secondary reactions at the surface of the Li_2CO_3 particles which slows down the rapid dissolution process. This proposition, to some extent, is supported by the leaching data since, if all species are using the same network of channels and the Mg ions display Fickian behaviour then it would be expected that Li ions would show similar behaviour, however, they are not showing this behaviour. Instead there is a considerable number of Li_2CO_3 particles remaining in the primer suggesting lower solubility for these particles which could be explained by a insoluble surface layer.

Finally, it is interesting to consider whether the leaching behaviour is the sum of leaching from a number of independent clusters of particles or whether the void networks develop in such a way that all particles are eventually involved. The SEM results of Fig. 4 and EDS results of Fig. 5 suggest that for most of the exposure times observed here that independent clusters do exist, since there are often very local changes observed deep within the primer. Even after 500 h exposure to NSS there are still many smaller Li_2CO_3 particles adjacent to depleted regions in the primer; these would be expected to dissolve if there is a widespread network in the primer (or if Li ions could diffuse through the PU matrix). The formation of these clusters, however, seems to partially involve rupture of the polyurethane due to internal stress around isolated particles particularly at short immersion exposure times. The buildup of internal stresses is likely to be greatest around the most soluble particles since the osmotic pressure and particle swelling are proposed to develop around most soluble particles which act as stress raisers. In this case the most soluble particles are the Li_2CO_3 particles. However, it can involve the MgO particles as well which can also act as stress raisers. Thus for this aspect of network formation all that is required is a “cluster” of stress raisers for transfer of the strain to the polyurethane matrix causing rupture and network formation. These results also suggest that, at longer exposure times, the void networks

associated with individual clusters may begin to merge to form larger structures which influence larger volumes of the primer. This is reflected in the leaching data where Fickian diffusion exhibited by Mg and Ba ions at intermediate times changes to diffusion slower than Fickian associated with the development of more complex diffusion paths through a structure with a fractal nature. (The more distributed the network then the lower the fractal index.) Presumably extensive network development co-incides with significant degradation of the primer.

5. Conclusions

Leaching studies have shown that for a polyurethane-based primer incorporating Li_2CO_3 and inorganic components such as MgO, $BaSO_4$ and TiO_2, Mg and Ba are both leached from the primer in addition to very high initial levels of Li release. SEM studies showed that as a result of Neutral Salt Spray exposure there appears to the initial, very high Li ion release is associated with surface dissolution (typically up to 5 μm). Following release of most of the Li from the surface, Mg release and lower levels of Ba release are observed. The release kinetics for Mg and Ba that displayed a t^n behavior where n was between 0.6 and 0.8. This indicates a mixture of Fickian diffusion and direct dissolution. SEM/EDS analyses of sections of the primer exposed to NSS showed that release is accompanied by delamination and dissolution around all types of particles including Li_2CO_3 particles which is observed deeper in the coating with increasing time. There was also rupture of the polyurethane matrix which facilitated the formation of networks penetrating the primer thickness to the polyurethane/metal interface. Finite element analyses indicated that rupture of the polyurethane could be due to the buildup of internal stresses in the coating resulting from osmotic effects and swelling around soluble particles. At the longest times there were considerable changes to the MgO and Li_2CO_3 particles such that there was near complete surface depletion of both types of particles. SEM results suggested that void networks that developed in the primer were involved interfaces of all particles. Leaching from these structures was slow and typical of restricted transport through a porous network. Particle Induced γ- and X-ray emission spectroscopy studies show that a Li and Mg depletion zones penetrated from the surface into the bulk of the primer at longer Neutral Salt Spray exposure times.

References

[1] R.G. Buchheit, A.E. Hughes, chromate and chromate-free coatings, in: C. Moosbrugger (Ed.), Corrosion: Fundamentals, Testing and Protection, ASM International, Mterials Park, Oh, USA, 2003, pp. 720–735.
[2] M.W. Kendig, R.G. Buchheit, Corrosion inhibition of aluminum and aluminum alloys by soluble chromates, chromate coatings, and chromate-free coatings, Corrosion 59 (2003) 379–400.
[3] J. Sinko, Challenges of chromate inhibitor pigments replacement in organic coatings, Prog. Org. Coat. 42 (2001) 267–282.
[4] A.E. Hughes, I.S. Cole, T.M. Muster, R.J. Varley, Combining green and self healing for a new generation of coatings for metal protection, Nat. Asia Mater. 2 (2010) 143–151.
[5] M. Zheludkevich, M. Ferreira, S. Poznyak, Self-Healing Corrosion Protection Coatings With Nanocontainers of Corrosion Inhibitors, (2007).
[6] M.L. Zheludkevich, I.M. Salvado, M.G.S. Ferreira, Sol-gel coatings for corrosion protection of metals, J. Mater. Chem. 15 (2005) 5099–5111.
[7] M.L. Zheludkevich, D.G. Shchukin, K.A. Yasakau, H. Mohwald, M.G.S. Ferreira, Anticorrosion coatings with self-healing effect based on nanocontainers impregnated with corrosion inhibitor, Chem. Mater. 19 (2007) 402–411.
[8] D.G. Shchukin, M. Zheludkevich, K. Yasakau, S. Lamaka, M.G.S. Ferreira, H. Mohwald, Layer-by-layer assembled nanocontainers for self-healing corrosion protection, Adv. Mater. 18 (2006) 1672.
[9] V. Jaskova, A. Kalendova, Anticorrosive coatings containing modified phosphates, Prog. Org. Coat. 75 (2012) 328–334.
[10] S.J. Garcia, H.R. Fischer, P.A. White, J. Mardel, Y. Gonzalez-Garcia, J.M.C. Mol, A.E. Hughes, Self-healing anticorrosive organic coating based on an encapsulated water reactive silyl ester: synthesis and proof of concept, Prog. Org. Coat. 70 (2011) 142–149.
[11] A.E. Hughes, 8 - self-healing coatings, in: G. Li, H. Meng (Eds.), Recent Advances in Smart Self-Healing Polymers and Composites, Woodhead Publishing, 2015, pp. 211–241.
[12] P. Visser, H. Terryn, J.M.C. Mol, Aerospace coatings, Springer Series in Materials Science, (2016), pp. 315–372.
[13] O. Gharbi, S. Thomas, C. Smith, N. Birbilis, Chromate replacement: what does the future hold? NPJ Mater. Degrad. 2 (2018) 12.
[14] P. Visser, Y. Gonzalez-Garcia, J.M.C. Mol, H. Terryn, Mechanism of passive layer formation on AA2024-T3 from alkaline lithium carbonate solutions in the presence of sodium chloride, J. Electrochem. Soc. 165 (2018) C60–C70.
[15] J.S. Laird, A.E. Hughes, C.G. Ryan, P. Visser, H. Terryn, J.M.C. Mol, Particle induced gamma and X-ray emission spectroscopies of lithium based alloy coatings, Nucl. Instrum. Methods Phys. Res. B 404 (2017) 167–172.
[16] P. Visser, A. Lutz, J.M.C. Mol, H. Terryn, Study of the formation of a protective layer in a defect from lithium-leaching organic coatings, Prog. Org. Coat. 99 (2016) 80–90.
[17] Y. Liu, P. Visser, X. Zhou, S.B. Lyon, T. Hashimoto, A. Gholinia, G.E. Thompson, G. Smyth, S.R. Gibbon, D. Graham, J.M.C. Mol, H. Terryn, An investigation of the corrosion inhibitive layers generated from lithium oxalate-containing organic coating on AA2024-T3 aluminium alloy, Surf. Interface Anal. 48 (2016) 798–803.
[18] P. Visser, Y. Liu, H. Terryn, J.M.C. Mol, Lithium salts as leachable corrosion inhibitors and potential replacement for hexavalent chromium in organic coatings for the protection of aluminum alloys, J. Coat. Technol. Res. 13 (2016) 557–566.
[19] Y. Liu, P. Visser, X. Zhou, S.B. Lyon, T. Hashimoto, M. Curioni, A. Gholinia, G.E. Thompson, G. Smyth, S.R. Gibbon, D. Graham, J.M.C. Mol, H. Terrynb, Protective film formation on AA2024-T3 Aluminum Alloy by leaching of lithium carbonate from an organic coating, J. Electrochem. Soc. 163 (2016) C45–C53.
[20] P. Visser, Y. Liu, X. Zhou, T. Hashimoto, G.E. Thompson, S.B. Lyon, L.G.J. Van Der Ven, A.J.M.C. Mol, H.A. Terryn, The corrosion protection of AA2024-T3 aluminium alloy by leaching of lithium-containing salts from organic coatings, Faraday Discuss. 180 (2015) 511–526.
[21] M.L. Zheludkevich, A.E. Hughes, Delivery systems for self healing protective coatings, Springer Series in Materials Science, (2016), pp. 157–199.
[22] K. Marcoen, P. Visser, G.F. Trindade, M.L. Abel, J.F. Watts, J.M.C. Mol, H. Terryn, T. Hauffman, Compositional study of a corrosion protective layer formed by leachable lithium salts in a coating defect on AA2024-T3 aluminium alloys, Prog. Org. Coat. 119 (2018) 65–75.
[23] S.P.V. Mahajanarn, R.G. Buchheit, Characterization of inhibitor release from Zn-Al-V10O28 (6-) hydrotalcite pigments and corrosion protection from hydrotalcite-pigmented epoxy coatings, Corrosion 64 (2008) 230–240.
[24] S.P.V. Mahajanam, R.G. Buchheit, Characterization of Zn-Al-V10O286- corrosion-inhibiting hydrotalcite pigments in epoxy resins, in: R.G. Buchheit, R.G. Kelly, N.A. Missert, B.A. Shaw (Eds.), Corrosion and Protection of Light Metal Alloys, 2004, pp. 270–282.
[25] R.G. Buchheit, H. Guan, Formation and characteristics of Al-Zn hydrotalcite coatings on galvanized steel, JCT Res. 1 (2004) 277–290.
[26] R.G. Buchheit, S.B. Mamidipally, P. Schmutz, H. Guan, Active corrosion protection in Ce-modified hydrotalcite conversion coatings, Corrosion 58 (2002) 3–14.
[27] M. Kendig, M. Hon, A hydrotalcite-like pigment containing an organic anion corrosion inhibitor, Electrochem. Solid State Lett. 8 (2005) B10–B11.
[28] H.N. McMurray, G. Williams, Inhibition of filiform corrosion on organic-coated aluminum alloy by hydrotalcite-like anion-exchange pigments, Corrosion 60 (2004) 219–228.
[29] G. Williams, H.N. McMurray, Inhibition of filiform corrosion on polymer coated AA2024-T3 by hydrotalcite-like pigments incorporating organic anions, Electrochem. Solid State Lett. 7 (2004) B13–B15.
[30] G. Williams, H.N. McMurray, Anion-exchange inhibition of filiform corrosion on organic coated AA2024-T3 aluminum alloy by hydrotalcite-like pigments, Electrochem. Solid State Lett. 6 (2003) B9–B11.
[31] A. Kumar, A. Kanta, N. Birbilis, T. Williams, B.C. Muddle, A pseudoboehmite-silane hybrid coating for enhanced corrosion protection of AA2024-T3, J. Electrochem. Soc. 157 (2010) C346–C356.
[32] D. Altenpohl, Corrosion 15 (1966) 143t.
[33] Vermilye Da, W. Vedder, Inhibition of aluminum + water reaction, Trans. Faraday Soc. 66 (1970) 2644.
[34] J.D. Gorman, A.E. Hughes, D. Jamieson, P.J.K. Paterson, Oxide formation on aluminium alloys in boiling deionised water and NaCl, CeCl3 and CrCl3 solutions, Corros. Sci. 45 (2003) 1103–1124.
[35] P. Klomjit, R.G. Buchheit, Characterization of inhibitor storage and release from commercial primers, Prog. Org. Coat. 114 (2018) 68–77.
[36] E. Javierre, S.J. García, J.M.C. Mol, F.J. Vermolen, C. Vuik, S. Van Der Zwaag, Tailoring the release of encapsulated corrosion inhibitors from damaged coatings: controlled release kinetics by overlapping diffusion fronts, Prog. Org. Coat. 75 (2012) 20–27.
[37] J. Mardel, S.J. Garcia, P.A. Corrigan, T. Markley, A.E. Hughes, T.H. Muster, D. Lau, T.G. Harvey, A.M. Glenn, P.A. White, S.G. Hardin, C. Luo, X. Zhou, G.E. Thompson, J.M.C. Mol, The characterisation and performance of Ce(dbp)3-inhibited epoxy coatings, Prog. Org. Coat. 70 (2011) 91–101.
[38] F.H. Scholes, S.A. Furman, A.E. Hughes, T. Nikpoura, N. Wrighta, P.R. Curtis, C.M. Macrae, S. Intem, A.J. Hill, Chromate leaching from inhibited primers - part I. Characterisation of leaching, Prog. Org. Coat. 56 (2006) 23–32.
[39] S.A. Furman, F.H. Scholes, A.E. Hughes, D. Lau, Chromate leaching from inhibited primers - part II: modelling of leaching, Prog. Org. Coat. 56 (2006) 33–38.
[40] T. Prosek, D. Thierry, A model for the release of chromate from organic coatings, Prog. Org. Coat. 49 (2004) 209–217.
[41] A.E. Hughes, A. Trinchi, F.F. Chen, Y.S. Yang, I.S. Cole, S. Sellaiyan, J. Carr, P.D. Lee, G.E. Thompson, T.Q. Xiao, Revelation of intertwining organic and inorganic fractal structures in polymer coatings, Adv. Mater. 26 (2014) 4504–4508.
[42] V.B. Mišković-stanković, D.M. Dražić, M.J. Teodorović, Electrolyte penetration through epoxy coatings electrodeposited on steel, Corros. Sci. 37 (1995) 241–252.

[43] I.M. Zin, R.L. Howard, S.J. Badger, J.D. Scantlebury, S.B. Lyon, The mode of action of chromate inhibitor in epoxy primer on galvanized steel, Prog. Org. Coat. 33 (1998) 203–210.
[44] V.B. Mišković-Stanković, M.R. Stanić, D.M. Dražić, Corrosion protection of aluminium by a cataphoretic epoxy coating, Prog. Org. Coat. 36 (1999) 53–63.
[45] A. Foyet, T.H. Wu, A. Kodentsov, L.G.J. van der Ven, G. de With, R.A.T.M. van Benthem, Absorption of water and corrosion performance of a clear and pigmented epoxy coating on Al-2024 alloy, Coat. Corros. Protect. 25 (2010) 31–39.
[46] J.M. Hu, J.Q. Zhang, C.N. Cao, Determination of water uptake and diffusion of Cl-ion in epoxy primer on aluminum alloys in NaCl solution by electrochemical impedance spectroscopy, Prog. Org. Coat. 46 (2003) 273–279.
[47] J. Kittel, N. Celati, M. Keddam, H. Takenouti, Influence of the coating–substrate interactions on the corrosion protection: characterisation by impedance spectroscopy of the inner and outer parts of a coating, Prog. Org. Coat. 46 (2003) 135–147.
[48] G.M. Geise, D.R. Paul, B.D. Freeman, Fundamental water and salt transport properties of polymeric materials, Prog. Polym. Sci. 39 (2014) 1–42.
[49] S. Mondal, J.L. Hu, Z. Yong, Free volume and water vapor permeability of dense segmented polyurethane membrane, J. Memb. Sci. 280 (2006) 427–432.
[50] M.F. Ferreira Marques, C. Lopes Gil, P.M. Gordo, Z. Kajcsos, A.P. de Lima, D.P. Queiroz, M.N. de Pinho, Free-volume studies in polyurethane membranes by positron annihilation spectroscopy, Radiat. Phys. Chem. 68 (2003) 573–576.
[51] S. Sellaiyan, A.E. Hughes, S.V. Smith, A. Uedono, J. Sullivan, S. Buckman, Leaching properties of chromate-containing epoxy films using radiotracers, PALS and SEM, Prog. Org. Coat. 77 (2014) 257–267.
[52] S.A. Furman, F.H. Scholes, A.E. Hughes, D.N. Jamieson, C.M. Macrae, A.M. Glenn, Corrosion in artificial defects. II. Chromate reactions, Corros. Sci. 48 (2006) 1827–1847.
[53] Z. Tabor, P. Warszyński, Modeling dissolution controlled release of inhibitor from a damaged coating, Corros. Sci. 82 (2014) 290–296.
[54] D.R. Jenkins, A.D. Miller, A model of chromate leaching from inhibited primers, 18th World IMACS/MODSIM Congress (2009).
[55] B.R. Hinderliter, S.G. Croll, D.E. Tallman, Q. Su, G.P. Bierwagen, Interpretation of EIS data from accelerated exposure of coated metals based on modeling of coating physical properties, Electrochim. Acta 51 (2006) 4505–4515.
[56] M. Musiani, M.E. Orazem, N. Pébère, B. Tribollet, V. Vivier, Determination of resistivity profiles in anti-corrosion coatings from constant-phase-element parameters, Prog. Org. Coat. 77 (2014) 2076–2083.
[57] S. Ranade, M. Forsyth, M.Y.J. Tan, In situ measurement of pipeline coating integrity and corrosion resistance losses under simulated mechanical strains and cathodic protection, Prog. Org. Coat. 101 (2016) 111–121.
[58] S. Amand, M. Musiani, M.E. Orazem, N. Pébère, B. Tribollet, V. Vivier, Constant-phase-element behavior caused by inhomogeneous water uptake in anti-corrosion coatings, Electrochim. Acta 87 (2013) 693–700.
[59] F. Mansfeld, M.W. Kendig, S. Tsai, Evaluation of corrosion behaviour of coated metals with AC impedance measurements, Corrosion 38 (1982) 478–485.
[60] A.E. Hughes, S. Yang, B. Oezkaya, O. Ozcan, G. Grundmeier, Physico-chemical characterisation of protective coatings and self healing processes, in: A.E. Hughes, J.M.C. Mol, M.L. Zheludkevich, R.G. Buchheit (Eds.), Active Protective Coatings: New-Generation Coatings for Metals, Springer, Netherlands, Dordrecht, 2016, pp. 241–298.
[61] S.D. Ranade, T. Hughes, S. Yang, M. Forsyth, J. Li, H. Wang, M.Y. Tan, Visualizing the impact of mechanical strain and the environment on pipeline coatings from a three dimensional perspective, Progr. Org. Coat. 122 (2018) 45–55.
[62] S. Ranade, M. Forsyth, M.Y.J. Tan, The initiation and propagation of coating morphological and structural defects under mechanical strain and their effects on the electrochemical behaviour of pipeline coatings, Progr. Org. Coat. 110 (2017) 62–77.
[63] C. Vosgien Lacombre, G. Bouvet, D. Trinh, S. Mallarino, S. Touzain, Effect of pigment and temperature onto swelling and water uptake during organic coating ageing, Progr. Org. Coat. 124 (2018) 249–255.
[64] C. Vosgien Lacombre, G. Bouvet, S. Cohendoz, D. Trinh, X. Feaugas, S. Touzain, S. Mallarino, Influence of internal stresses on the physicochemical and mechanical properties evolution of pigmented epoxy systems during hygrothermal ageing, Surf. Coat. Technol. 341 (2018) 86–94.
[65] M. Fernández-García, M.Y.M. Chiang, Effect of hygrothermal aging history on sorption process, swelling, and glass transition temperature in a particle-filled epoxy-based adhesive, J. Appl. Polym. Sci. 84 (2002) 1581–1591.
[66] D.Y. Perera, Effect of pigmentation on organic coating characteristics, Progr. Org. Coat. 50 (2004) 247–262.
[67] A.D. King, J.S. Lee, J.R. Scully, Finite element analysis of the galvanic couple current and potential distribution between Mg and 2024-T351 in a Mg rich primer configuration, J. Electrochem. Soc. 163 (2016) C342–C356.
[68] D.R. Lide, CRC Handbook of Chemistry and Physics, CRC Press, Boston, 1990.
[69] I.J. Polmear, Light Allopys: Metallurgy of the Light Metals, 3rd ed., Arnold, London, 1995.
[70] C.G. Ryan, D.N. Jamieson, W.L. Griffin, G. Cripps, R. Szymanski, The new CSIRO-GEMOC nuclear microprobe: first results, performance and recent applications, Nucl. Instrum. Methods Phys. Res. B 181 (2001) 12–19.
[71] X. Wu, K. Hebert, Development of surface impurity segregation during dissolution of aluminum, J. Electrochem. Soc. 143 (1996) 83–91.
[72] C. Boni, E. Cereda, G.M.B. Marcazzan, V. De Tomasi, Prompt gamma emission excitation functions for PIGE analysis, Nucl. Instrum. Methods Phys. Res. B 35 (1988) 80–86.
[73] M. Kitano, M. Shiojiri, Bénard convection ZnO/resin lacquer coating — a new approach to electrostatic dissipative coating, Powder Technol. 93 (1997) 267–273.
[74] C.M. Hansen, P.E. Pierce, Surface effects in coatings processes, Ind. Eng. Chem. 13 (1974) 218–225.
[75] A.E. Hughes, J.S. Laird, C.G. Ryan, P. Visser, H. Terryn, J.M.C. Mol, Particle characterisation and depletion of Li_2CO_3 inhibitor in a polyurethane coating, Coatings 7 (2017).
[76] R.C. Carson, J. Simandl, Kinetics of magnesium hydroxide precipitation from seawater using slaked dolomite, Miner. Eng. 7 (1994) 511–517.
[77] Q. Yuan, Z. Lu, P. Zhang, X. Luo, X. Ren, T.D. Golden, Study of the synthesis and crystallization kinetics of magnesium hydroxide, Mater. Chem. Phys. 162 (2015) 734–742.
[78] Y. Dong, Q. Zhou, Relationship between ion transport and the failure behavior of epoxy resin coatings, Corros. Sci. 78 (2014) 22–28.
[79] J. Mähler, I. Persson, A study of the hydration of the alkali metal ions in aqueous solution, Inorg. Chem. 51 (2012) 425–438.
[80] M.H. Shirangi, X.J. Fan, B. Michel, Mechanism of moisture diffusion, hygroscopic swelling and adhesion degradation in Epoxy Molding Compounds, Proceedings - 2008 International Symposium on Microelectronics (2008) 1082–1089.
[81] J. Wang, D.S. Dlamini, A.K. Mishra, M.T.M. Pendergast, M.C.Y. Wong, B.B. Mamba, V. Freger, A.R.D. Verliefde, E.M.V. Hoek, A critical review of transport through osmotic membranes, J. Memb. Sci. 454 (2014) 516–537.
[82] P. Carbonini, T. Monetta, L. Nicodemo, P. Mastronardi, B. Scatteia, F. Bellucci, Electrochemical characterisation of multilayer organic coatings, Prog. Org. Coat. 29 (1996) 13–20.
[83] C. Vosgien Lacombre, G. Bouvet, D. Trinh, X. Feaugas, S. Touzain, S. Mallarino, Influence of pigment and internal stresses on water uptake in model epoxy: a thermodynamic approach, J. Mater. Sci. 53 (2018) 2253–2267.